Master's thesis

NTNU
Norwegian University of Science and Technology
Faculty of Natural Sciences
Department of Physics

Hanne Maren Helgedagsrud

Estimation of nonlinear bulk elasticity parameter for cancer tumors

Master's thesis in Physics and Mathematics
Supervisor: Rune Hansen
May 2021

NTNU
Norwegian University of
Science and Technology

Hanne Maren Helgedagsrud

Estimation of nonlinear bulk elasticity parameter for cancer tumors

Master's thesis in Physics and Mathematics
Supervisor: Rune Hansen
May 2021

Norwegian University of Science and Technology
Faculty of Natural Sciences
Department of Physics

NTNU
Kunnskap for en bedre verden

Abstract

Dual frequency ultrasound has been used to estimate the nonlinear elasticity parameter of pancreatic ductal adenocarcinoma (PDAC) tumors, the most common type of pancreatic cancer. The tumors have grown in KPC mice, but the measurements have been *in vitro*. As a validation of the obtained estimates, the nonlinear bulk elasticity parameter has been estimated for healthy organs from KPC mice and compared with literature values.

The average nonlinear bulk elasticity of all tumors has been estimated to be 1.53 GPa^{-1} at room temperature and 1.31 GPa^{-1} at body temperature with a precision of 95.8 %. The same estimation has been performed on healthy tissue where an accuracy of 87.0 % or higher are observed, when comparing the estimated value of the healthy organs with literature values from human organs.

The *in vitro* studies have been carried out using the programmable scanner "Verasonics", and the radio frequency signal has been processed using MATLAB.

Measurements have been made for tumors and organs being fresh as well as tempered after being frozen. No consistent correlation has been found between the nonlinear elasticity parameter and the number of times it has been frozen. The temperature has been varied from 20 °C to 38 °C and has shown a tendency of decreasing nonlinear elasticity parameter for increasing temperature.

Sammendrag

Tofrekvens-ultralyd har blitt brukt til å estimere ikke-lineær bulk elastisitet for adenokarsinom i bukspyttkjertelen (PDAC svulst), den vanligste krefttypen i bukspyttkjertelen. Svulstene har vokst i KPC-mus, men målingene er gjennomført *in vitro*. Som en validering av de estimerte verdiene ble den samme metoden brukt på friske organer fra mus og sammenliknet med tilgjengelige litteratureverdier.

Ikke-lineær bulk elastisitet for svulstene ble estimert til 1.53 GPa^{-1} ved romtemperatur og 1.31 GPa^{-1} ved kroppstemperatur, med en presisjon på 95.8 %. Ved å sammenlikne estimerte verdier for de friske organene med litteratureverdier fra friskt menneskevev ble nøyaktigheten for metoden beregnet til å være fra 87.0 % og høyere.

In vitro målingene ble utført med den programmerbare skanneren "Verasonics" og radiofrekvenssignalene er behandlet ved hjelp av MATLAB.

Målingene ble gjort på ferske svulster og organer, samt svulster og organer som har vært fryst. Det ble ikke funnet noen konsistent sammenheng mellom den ikke-lineære bulk elastisiteten og antall ganger svulsten eller organet har vært fryst. Temperaturen ble variert fra 20 °C til 38 °C, og viste en tendens til at den ikke-lineær bulk elastisiteten reduseres når temperaturen øker.

Preface

I started at the Master's Degree Programme within Applied Physics and Mathematics in Trondheim based on my interest in physics and mathematics and lack of knowing what I wanted to work with when I grew up. The first two years felt like adding tools to my toolbox by doing general courses in mathematics and physics. In the third year I chose biophysics and medical technology as my main profile. In the course *Cell biology and cellular biophysics* covered by Catharina De Lange Davies, I found cancer cells to be very fascinating. Their ability to survive and spread caught my mind.

In my fourth year of studies, I exchanged one year in Denmark at the Technical University of Denmark. Here, I got interested in medical imaging techniques after a course covered by Jørgen Jensen. It was exciting to learn how physics is applied, combined with signal processing and programming, to analyze the results.

In October 2020 I got in contact with Bjørn Atle Anglelsen and Naseh Amini, working on ultrasound and cancer medicine. Together, we designed what was going to be the content of my master thesis, the crown of my studies.

The content turned out to be the best of all worlds; fighting cancer, programming and ultrasound imaging.

Acknowledgements

Many people have contributed in different ways to make it possible for me to finish my studies in applied physics and mathematics.

First of all, I want to thank my supervisors for the help with my thesis. It all started with Bjørn Atle Anglelsen who helped me define the thesis and getting the right people involved. Rune Hansen has been my main supervisor along the way. He helped me understanding the theory and making the structure of the thesis. Naseh Amini gave me an introduction to the Verasonics scanner and helped me with the first experiments. Stian Solberg has helped me with analyzing the data from the experiments. He has been unusually good at answering my many questions – both at Mondays at 08.00 but also at Saturday evenings. Einar Sulheim has provided me with tumors and organs from mice. They have all shared knowledge and supported me along the way.

Furthermore, I want to thank my family for their support and motivation. It should also be mentioned that they made it possible for me to continue my passion for competing in showjumping alongside the studies.

Finally, I want to thank all the nice people I have been lucky to meet during my studies. I feel privileged to have been a part of the lovely life of the students in Trondheim.

Contents

Nomenclature

Abbreviations

BM	Basement membrane
DNA	Deoxyribonucleic Acid
EC	Endothelial cell
EF	Estimation functiona
f0	Frozen zero times (i.e. fresh)
f1	Frozen one time
f2	Frozen two times
FWHM	Full-width half maximum
HF	High frequency
KPC	Kras,p53,Cre
LF	Low frequency
NEP	Nonlinear elasticity parameter
NPD	Nonlinear propagation delay
PDAC	Pancreatic ductal adenocarcinoma
PRF	Pulse repetition frequency
RF	Radio frequency

SURF Second order ultrasound field

T Temperature

VEGF Vascular endothelial growth factor

Symbols

β NEP

β_{n} Nonlinearity parameter

δ_{t} Time step

$\Gamma(\mathrm{r})$ Transmit beam axis

$\hat{\mathrm{y}}_{+}$ HF receive signal for a positive polarity

$\hat{\mathrm{y}}_{-}$ HF receive signal for a negative polarity

$\hat{\mathrm{y}}_{0}$ HF receive signal for a zero polarity

κ_{s} Isentropic volume compressibility

ω_{c} Center frequency

ϕ Phase

ρ_0 Mass density of uncompressed material

τ First order NPD

τ_{+} Positive polarity of NPD

τ_{-} Negative polarity of NPD

τ_{n} Noisy NPD

τ_{x} Modeled NPD

τ_{y} Measured NPD

$\mathrm{c_p}$ Specific heat capacity

f_0 Transducer center frequency

$\mathrm{W_D}$ Distance weight

$\mathrm{W_R}$ Regularization weight

$y_0(t)$	Analytic signals with zero-polarity
$y_p(t)$	Analytic signals with nonzero-polarity
a	Amplitude
A,B	Material parameters
c_0	Linear low amplitude propagation velocity
h	Heat transfer coefficient
k	Constant in Newtons law of heating
M	Contact area
p	Local acoustic pressure
r	Radius
S	Entropy
z	Depth

Chapter 1

Introduction

The overall goal of this thesis is to find the nonlinear bulk elasticity for pancreatic cancer tumors. Tumors are denser than soft tissues, which in theory means that the bulk elasticity is lower. Literature values do exist for healthy tissues, but not for tumors. This means that the estimation has to be validated based on results from healthy tissues.

An imaging technique introduced in 2007 known as second order ultrasound field (SURF) imaging is used, Here, dual frequency ultrasound is used and the nonlinear bulk elasticity is imaged rather than the scatter response of tissues as for conventional ultrasound imaging. As the bulk elasticity is higher for softer tissues, the hypothesis is that tumors will show contrast to healthy tissues and hence appear as darker areas in the images.

The measurements are made in very controlled surroundings, where a tumor is placed in a box of salty water. The results from this thesis can therefore be used as an indication of the nonlinear bulk elasticity values. However, the final answer of whether or not the tumors are visible, can first be answered after measurements of tumors integrated with tissues have been made. This is mainly because the noise is very low in the box of water compared to the tumor being located inside tissues. To get an impression of how accurate the method is, data from healthy tissues will also be collected. In this way, the value of the nonlinear bulk elasticity itself can be validated as literature values exist, but the combination of tumor and healthy tissues in the same measurements will remain unanswered.

The measurements are made in varying temperatures and on both fresh tumors and tumors that have been frozen to see how the nonlinear bulk elasticity varies.

The structure of this thesis will be similar to a report, with a theory part, an experimental part, results, discussion and a conclusion. The chapters are as follows:

Chapter 1: The introduction.

Chapter 2: Presentation of cancer theory and the scope of this disease. In 2019, nearly 35 thousand new cancer cases were reported in Norway according to Cancer Registry of Norway. Worldwide in 2018, 18.1 million new cases and 9.5 million cancer-related deaths were reported according to National Cancer Institute. An elusive amount of money and work is and has been spent on fighting cancer.

Chapter 3: Introduction to bulk elasticity theory. Bulk elasticity describes how resistant material is to an external compression, which is highly relevant for this thesis where the material is molecules in tissue and the external compression are sound waves originating from the ultrasound transducer. One important parameter will be introduced; nonlinear bulk elasticity, β.

Chapter 4: Presentation of medical ultrasound theory with a focus on SURF imaging and dual frequency ultrasound. In short, dual frequency ultrasound means that the signal is composed of a low frequency (LF) pulse and a high frequency (HF) pulse. The LF pulse affects the medium and the HF pulse such that a measurable time delay τ occurs. This delay is proportional to β.

Chapter 5: Details of the experiments and methods used. Illustrations and pictures of the experimental setup will be shown, in addition to tables with detailed information of all measurements which has been made. The Versonics scanner will be presented, which is a program that can be used in studies with dual frequency measurements since it can be programmed by the user. Different versions of MATLAB code used to analyze the results will also be presented.

Chapter 6: Presentation of the results. The first measurements were used to optimize the method, while the rest of the measurements were used to estimate β. Results used to modify the method, calculations necessary to estimate β and figures showing the estimated β values for all tumors and organs are presented in the chapter.

Chapter 7: Discussion of the results. Sources of error, precision, accuracy, artefacts and temperature dependency are some of the subjects discussed.

Chapter 8: Conclusion and future work. The second order ultrasound field (SURF) method where dual frequency ultrasound is a relatively new imaging technique with great potential and is used *in vitro* in this thesis. In this chapter the next step for the method is proposed, in addition to suggestions for improvement of the method.

Chapter 2

Cancer

Cancer is the second-leading case of death and arise because of abnormalities in cell functions (Hardin and bertoni (May 30, 2017)). Cancer cells have the ability to spread by invasion and metastasis, and make sure to get nutrition through angiogenesis. This makes cancer cells hard to overcome if they arise. However, cancer medicine has been researched for decades and early detection of cancer has shown to increase the probability of successful treatment (World Health Organization).

Sintef and NTNU have a project where the uptake of cancer medicine has shown to increase, when ultrasound is applied on air bubbles in the capillaries. A part of this project is to study the nonlinear bulk elasticity parameter of cancer tumors, which may result in early detection of tumors using ultrasound. Before presenting the nonlinear bulk elasticity parameter, cancer theory will by start be elaborated.

2.1 How cancer arise

Cancer cells arise from mutations in the body's own cells, leading to an abnormal type of tissue growth where the cells divide in an uncontrolled way. As a consequence, the balance between cell division and cell death is disrupted. 90 % of all cancers are carcinomas, which arise from epithelial cells covering external and internal body surfaces. Fig. 2.1 compares normal and tumor growth in the epithelium of the skin. In the basal lamina, stem cells divide on average into one new stem cell and one specialized cell. The stem cell remains in the basal lamina to divide again, while the specialized cell loses the capacity to divide and differentiates as it moves towards the outer skin. In the case of tumor growth, on the other hand, the balance between cell death and cell division is disrupted leading to a progressive increase in the number of dividing cells.

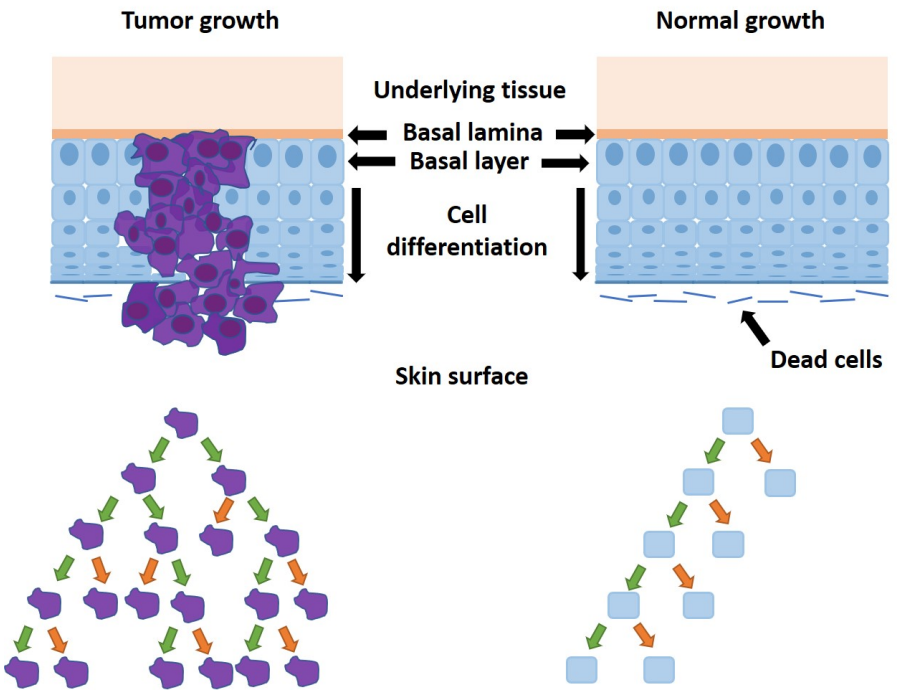

Figure 2.1: Illustration of how a tumor can grow in the epithelium if the cell differentiation is out of balance. In the basal layer in normal skin, the stem cells are on average divided into one that retains the capacity to divide (green arrow in the lower illustration) and one that differentiates and hence loses the ability to divide further (orange arrow in the lower illustration). In tumor growth, on the other hand, this balance is lost. As a result, the number of dividing cells increases progressively and gives rise to a tumor.

Other types of cancer categories are sarcomas, lymphomas and leukemias. Sarcomas develop from supporting tissues, such as bone, cartilage, fat and muscle. Lymphomas and leukemias arise from blood cells and cells from lymphatic organs.

2.2 How tumors grow

Experiments have shown that tumors need a blood supply to grow beyond 1-2 mm in size (Hardin and bertoni May 30, 2017). The blood supply is achieved through angiogenesis [1], which cancer cells can initialize. The process is illustrated in Fig. 2.2 (Vroling et al. 2007). First, angiogenic growth factors are released by the cancer cells and diffuse into nearby tissues. Specific receptors for the growth factors are vascular endothelial growth factor (VEGF) receptors located on the endothe-

[1] Angiogenesis is the term for the growth of blood vessels

lial cells (ECs). ECs will then be activating leading to the release of enzymes that dissolve holes in the basement membrane (BM) surrounding existing blood vessels. Furthermore, ECs will proliferate (divide) and migrate through the dissolved holes, corresponding to building a vessel towards the tumor. The vessel forms a loop through the tumor and is stabilized by smooth muscle cells.

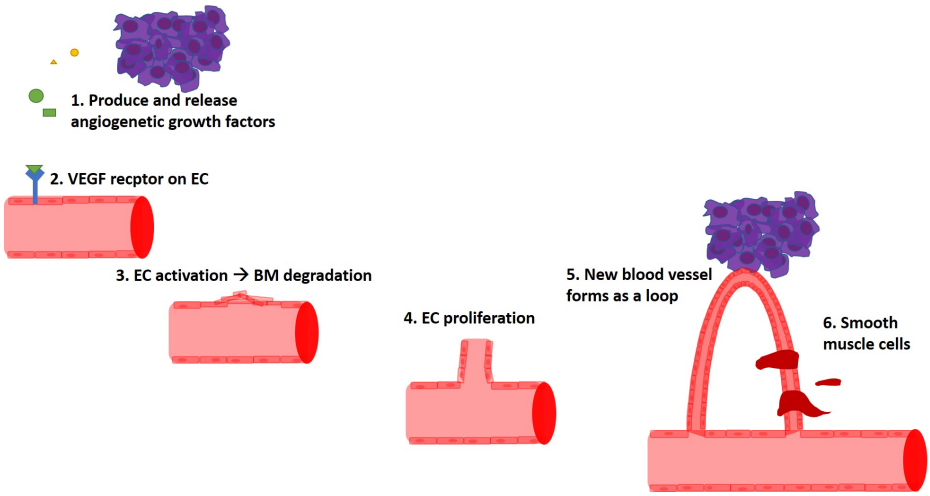

Figure 2.2: Cancer cells can initiate angiogenesis by releasing angiogenetic growth factors (1). In this way, the tumor gets nutrition and will grow in size. The growth factors will attach to vascular endothelial growth factor (VEGF) receptors on the endothelial cells (ECs) (2). In this way, the ECs are activated and start degrading the basement membrane (BM) (3). This results in holes in the BM, where ECs proliferate and migrate through (4). The new blood vessel forms a loop by the tumor and is stabilized by smooth muscle cells (5,6).

2.3 How cancer spread

Cancer cells have the ability to do metastasis, which is invading neighboring tissues and enter the bloodstream (Hardin and bertoni May 30, 2017). At distant sites, the cancer cells attach to the vessel wall and invade new sites. In this way, the tumors are spread throughout the body.

There are three stages of metastasis, illustrated in Fig. 2.3. The first step is invading surrounding tissues and vessels, the second is the penetration of the blood vessel wall and transportation by the bloodstream. The third and final step is the exit of the bloodstream and invasion of a new organ. This often takes place in the capillaries, because of the small diameter of the vessels. As a consequence, cancer often spreads to the lungs because this is the first network of capillaries from many organs. The liver is also a common site of metastasis, as this is the first

capillary bed for stomach and colon cancer. However, only a small fraction of the cancer cells are capable of doing all three steps, and hence complete a successful metastasis.

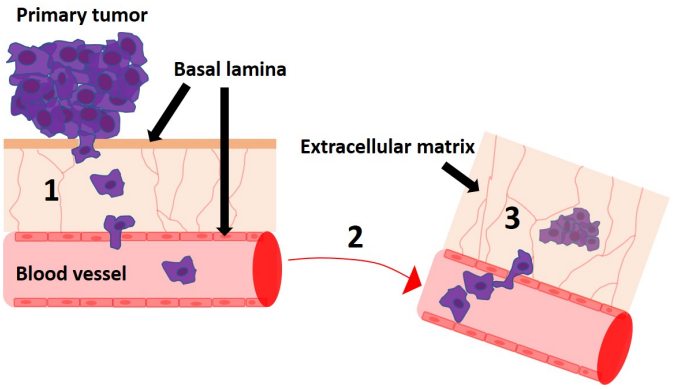

Figure 2.3: The three steps of metastasis, describing how cancer spreads. The cancer cells invade surrounding tissue (1) before penetrating a blood vessel. The bloodstream transports the cancer cells (2) in the circulatory system. The cancer cells may attach to the vessel wall and leave the bloodstream to grow at a new site (3).

2.4 How to treat cancer

National Cancer Institute lists many types of available cancer treatments. Some treatments are "local" (e.g. radiation therapy) and target a specific site in the body, while other treatments are "systematic" (e.g. chemotherapy) and can affect the entire body. The type of treatment depends on the type of cancer, which has attacked the body. Most people will be given a combination of treatments, but single treatments can also be given. Individual response to treatments makes fighting cancer difficult, and the side effects do also vary from person to person for the same treatment. Some examples of side effects are hair loss, appetite loss, pain, anemia, sleep problems, nerve problems, memory loss, skin change and diarrhea. Some examples of cancer treatments are:

2.4.1 Radiation therapy

Radiation therapy uses ionization radiation (e.g. X-rays) to kill cancer cells and shrink cancer tumors. The dose is much higher than the received dose during conventional X-ray imaging. When the received dose is high, the DNA of the cells are damaged, which will stop the cells to divide, or kill them. The cells are not killed immediately during radiation therapy, the process takes days or weeks of treatment.

2.4.2 Surgery

In surgery, cancer tumors, or part of cancer tumors, are removed from the body. The treatment works best for solid tumors before they undergo metastasis. The treatment does require the position of the tumor, and some nearby healthy tissue might also be removed.

2.4.3 Chemotherapy

Chemotherapy is a treatment where drugs are used to stop or slow down the growth of cancer cells and ease the symptoms and pain. Chemotherapy is typically combined with radiation therapy to decrease the tumor size before other treatments are performed or destroy the remaining cancer cells after the other treatments have been performed.

Chapter 3

Bulk elasticity

The bulk elasticity of materials describes how resistant the material is to external compression. Ultrasound waves are acoustic pressure waves and hence an external compression for tissues. Consequently, ultrasound can be used to estimate the bulk elasticity of the tissue. Bulk elasticity is characteristic of all materials, which makes it valuable in medical diagnostics.

For acoustic waves in solids and fluids, it is a common and convenient method to start with the equation of state for pressure waves where it is assumed that the pressure p is a function of mass density ρ and entropy S,

$$\mathrm{p} = \mathrm{p}(\rho, \mathrm{S})$$

This was early done by Fox and Wallace (1954) and Beyer (1960). By applying Taylor expansion at equilibrium density $\rho = \rho_0$ assuming isentropic conditions (constant entropy) the equation of state takes the form

$$\mathrm{p}(\rho) = \mathrm{p}(\rho_0) + \Big(\frac{\partial \mathrm{p}}{\partial \rho}\Big)_{\mathrm{S},\rho=\rho_0}\big(\rho - \rho_0\big) + \Big(\frac{\partial^2 \mathrm{p}}{\partial \rho^2}\Big)_{\mathrm{S},\rho=\rho_0}\frac{\Big(\rho - \rho_0\Big)^2}{2!} + ...$$

The subscript $\Big(\mathrm{S}, \rho = \rho_0\Big)$ indicates constant entropy and Taylor expansion at $\rho = \rho_0$.

The equation of state to the 2nd order can be simplified using two material parameters A and B, defined as

$$\mathrm{A} = \rho_0\Big(\frac{\partial \mathrm{p}}{\partial \rho}\Big)_{\mathrm{S},\rho=\rho_0} = \frac{1}{\kappa_\mathrm{s}} \tag{3.1}$$

and

$$\mathrm{B} = \rho_0^2 \Big(\frac{\partial^2 \mathrm{p}}{\partial \rho^2} \Big)_{\mathrm{S},\rho=\rho_0}$$

where κ_s is the isentropic volume compressibility. The equation of state becomes

$$\begin{aligned} \mathrm{p}(\rho) &= \mathrm{p}_0 + \mathrm{A}\frac{\rho-\rho_0}{\rho_0} + \frac{\mathrm{B}}{2}\Big(\frac{\rho-\rho_0}{\rho_0}\Big)^2 \\ &= \mathrm{p}_0 + \mathrm{A}\frac{\rho-\rho_0}{\rho_0}\left(1 + \frac{\mathrm{B}}{2\mathrm{A}}\Big(\frac{\rho-\rho_0}{\rho_0}\Big)\right) \end{aligned} \tag{3.2}$$

The term $\mathrm{A}\frac{\rho-\rho_0}{\rho_0}$ describes the linear bulk elasticity while the term $\frac{\mathrm{B}}{2\mathrm{A}}\Big(\frac{\rho-\rho_0}{\rho_0}\Big)$ describes the deviation from the linear bulk elasticity, in compliance with Hansen et al. (2011).

The next parameter to be introduced is the nonlinear elasticity parameter (NEP) β, which depends on the material parameters A and B. β is a commonly used symbol for the NEP, but other symbols may also occur. Xia (2019) use Γ as one example. However, we first define the nonlinearity parameter β_n as

$$\beta_\mathrm{n} = 1 + \frac{\mathrm{B}}{2\mathrm{A}}$$

which can be recognized from Eq. (3.2). Finally, the NEP β is defined like in Hansen et al. (2010) as

$$\beta = \beta_\mathrm{n}\kappa_\mathrm{s} \tag{3.3}$$

β is an important parameter due to its connection to acoustic properties of materials which makes it characteristic for tissue types. For cancer tumors, it is important to examine whether the cancer is malignant or not. Today, a common way of diagnosing cancer is by biopsy [1], but maybe a measurement of β has the same diagnostic value, with the advantage of not being invasive.

One method to estimate the NEP of materials is the usage of dual frequency ultrasound presented in Hansen et al. (2010). This SURF method is used in the experiments and will be further discussed in Section 4.2. The main idea, however, is that the ultrasound propagation velocity c(z, p) varies with the pressure p and depth z as

$$\mathrm{c(z,\,p)} \approx \mathrm{c}_0\mathrm{(z)}\big[1 + \beta\mathrm{(z)p(z)}\big] \tag{3.4}$$

[1] In biopsy a sample of tissue is taken from the body and examined in the laboratory.

where $c_0(z)$ is the linear low amplitude propagation velocity and $\beta(z)$ is the NEP, as before, at depth z. The approximation is valid when $\kappa_s p << 1$, as in diagnostic ultrasound imaging. $c_0(z)$ is defined as

$$c_0(z) = \frac{1}{\sqrt{\rho_0(z)\kappa_s(z)}} \tag{3.5}$$

Table 3.1 shows literature values for the introduced parameters from Mast (2000). The experiments were made in vitro, which leads to the assumption of values applying to room temperature as nothing else is specified.

Table 3.1: Table values for mass density of uncompressed material ρ_0, linear low amplitude propagation velocity c_0, and bulk elasticity parameters κ, β_n and β, with κ and β calculated using Eqs. (3.5) and (3.3) The values originate from Mast (2000) and are assumed to be true for room temperature.

	ρ_0 kg/m^3	c_0 m/s	κ GPa^{-1}	β_n -	β GPa^{-1}
Liver	1060	1595	0.371	4.3	1.59
Skeletal muscle	1050	1580	0.382	4.3	1.64
Brain	1040	1560	0.395	4.55	1.80
Kidney	1050	1560	0.391	4.7	1.84
Fatty	985	1465	0.473	5.25	2.48

Single frequency ultrasound for imaging β has been used in laboratory settings, but the method is only successful in transmission mode (Kvam et al. 2019). Using transmission mode the ultrasound propagates through the object and is received 180°relative to the transmitter. In this way quantitatively images of ultrasound velocity could be obtained, but the method would be limited to breast imaging due to difficulties with propagating ultrasound waves through other tissues. In pulse-echo mode, unreliable estimates are produced because of diffraction and speckle.

Chapter 4

Medical ultrasound

In this chapter, both general medical imaging ultrasound and dual frequency ultrasound will be presented. The last part will in many ways be a brief summary of the technique for estimating the nonlinear elasticity parameter (NEP) using dual frequency ultrasound invented by Hansen, Måsøy, Johansen, and Angelsen.

4.1 General ultrasound theory

Ultrasound is sound waves with frequencies above 20 kHz. According to Aladin Carovac and Junuzovic (2011), the first recorded application of ultrasound was the detection of submarines during World War I. It was not until after the 1950s it was applied for medical purposes. Today, ultrasound is used both for diagnostic and therapeutic purposes. Ultrasound systems are non-invasive, portable and relatively inexpensive.

Ultrasound makes matter vibrate mechanically and acts as a disturbance in the medium (Jensen August 30, 2013). Particles in the medium will oscillate around their mean position as illustrated in Fig. 4.1. Since no mass is transported, the net displacement of the particles is unchanged. If no wave disturbance was present, however, the particles would have been uniformly distributed and at rest.

The time it takes for the ultrasound beam to travel through the tissue, to be reflected, and then return to the transducer is given by t = 2d/c, where d is the depth of interaction and c is the speed of sound.

One wave has to return to the transducer before the next wave is transmitted. This is called the pulse repetition frequency, PRF = $1/t_{max}$, and depends on the maximum depth to be imaged. For imaging at a depth of 3 cm as an example, the PRF

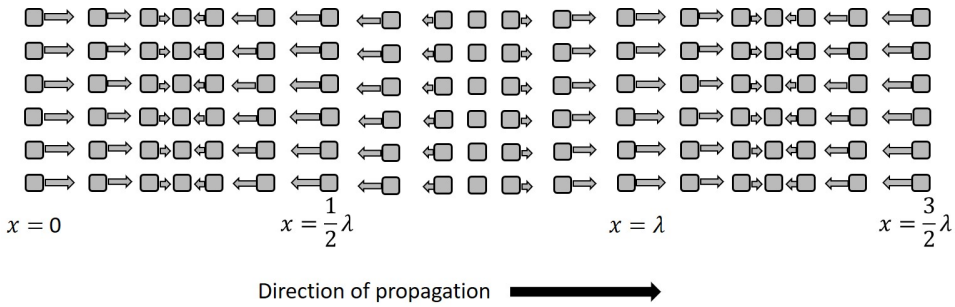

Figure 4.1: Particles in a medium oscillates around their mean position when a longitudinal wave is applied. The arrows correspond to magnitude and direction of the particle motion.

is

$$\text{PRF} = \frac{1}{\text{t}_{\text{max}}} = \frac{\text{c}}{2\text{d}} = \frac{1540\text{m/s}}{2 \cdot 0.03\text{m}} \approx 26\text{kHz}$$

An important part of the ultrasound transducer is the piezoelectric crystal, where mechanical and electrical energy can convert back and forth using the piezoelectric effect. This is how transducers receive and transmit sound waves.

When an electric field is applied to the crystal, the internal dipole structure will change and cause a vibration in the crystal. This converts electric energy to mechanical energy and describes how the transducers produce sound waves. The frequency of the vibration will correspond to the frequency of the sound wave, which is called the transducer center frequency f_0.

Most transducers are broadband, which means they can operate at a range of frequencies. A lower center frequency gives deeper penetration of materials, while a higher frequency reduces the penetration depth. f_0 is usually in the range 2 MHz (deep abdominal imaging) to 15 MHz (musculoskeletal imaging).

The same principle is used when the sound wave returns to the transducer, such that the mechanical energy is converted to electrical energy

There are two types of resolution to consider; axial and lateral. The axial resolution is the ability to distinguish points at different depths. Hence, the axial resolution is proportional to the wavelength λ. Since $\lambda \propto 1/\text{f}_0$, a good axial resolution is obtained at higher f_0. The lateral resolution is the ability to distinguish points at different widths. The full-width half maximum (FWHM) of the frequency range produced by the transducer is one measure of the lateral resolution. A smaller number of FWHM corresponds to a better image.

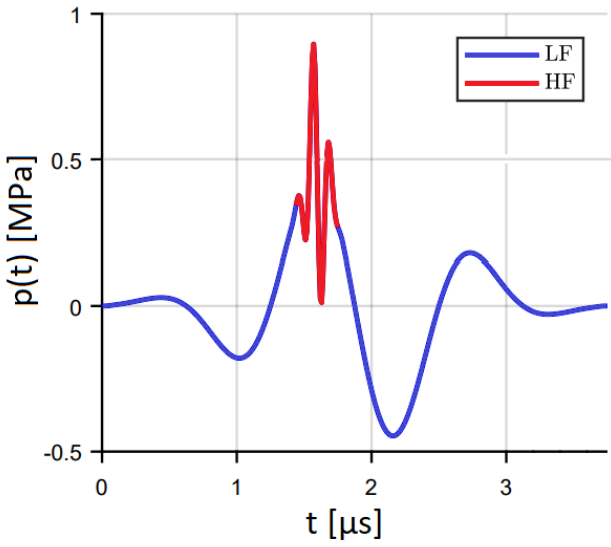

Figure 4.2: Dual frequency pulse complex composed of a high frequency (HF) pulse at 8MHz, and a low frequency (LF) pulse at 0.8MHz. The figure is adapted from Kvam et al. (2019).

4.2 Dual frequency ultrasound

In 2007, a new imaging technique called second order ultrasound field (SURF) was presented by Angelsen and Hansen. The method is applicable with pulse-echo acquisition which makes it possible to do *in vitro* scanning.

The technique is based on transmitting dual frequency pulse complexes composed of the conventional imaging high frequency (HF) pulse together with a modifying low frequency (LF) pulse. The LF pulse is said to have a positive polarity if the HF pulse is positioned on a crest of the LF pulse and a negative polarity if the HF pulse is positioned on the trough of the LF pulse. A zero polarity indicates no manipulation from the LF pulse. An example of a positive polarity complex is shown in Fig. 4.2

The total acoustic pressure p(z,t) of the transmitted pulse is given by

$$p(z,t) = p_L(z,t) + p_H(z,t) \tag{4.1}$$

where $p_L(z,t)$ is the acoustic pressure of the LF pulse at the center of the HF pulse and $p_H(z,t)$ is the acoustic pressure of the HF pulse at time t and depth z.

The LF pulse will compress or expand the medium and hence change the prop-

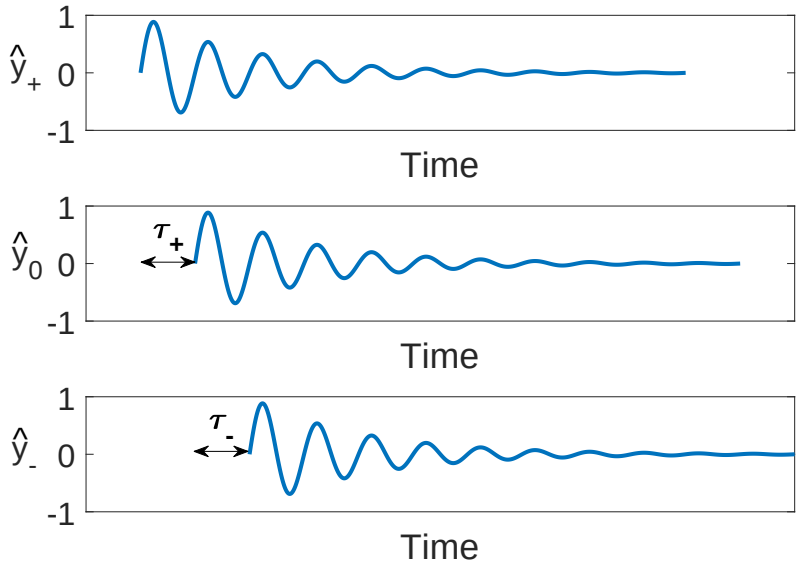

Figure 4.3: Typical HF receive signal for a positive polarity $\hat{y}_+$, zero polarity $\hat{y}_0$ and negative polarity $\hat{y}_-$. The corresponding delay between the signals are denoted in the figure as τ_+ and τ_-.

agation velocity of the HF pulse. By combining Eq. (4.1) and Eq. (3.4), the propagation velocity observed from the HF pulse becomes

$$c_H(z,t) = c_0(z)\Big(1 + \beta p_L(z,t) + \beta p_H(z,t)\Big) \tag{4.2}$$

One can see that the propagation velocity decreases if the polarity is negative, and increase if the polarity is positive. Consequently, a nonlinear propagation delay (NPD) between a zero-polarity and nonzero-polarity signal appears and increases with depth.

To make a visualization of the delay, Fig. 4.3 will be discussed. This figure shows typical HF receive signals at a given image depth z for different polarities of the LF pulse. For a positive polarity of the LF pulse, the material will be compressed (p>0) at the location of the HF pulse which increase the propagation velocity $c_H(t)$ and advance the arrival time relative to the zero polarity pulse, which also can be concluded using Eq. (4.2) and Eq. (4.3). For a negative polarity of the LF pulse, the opposite case will be observed. The material will be expanded (p<0) at the location of the HF pulse which decrease $c_H(z,t)$ and increase the arrival time. The polarity can also be zero, which results in no change in the material characteristics

and hence no change in $c_H(z,t)$ and arrival time. To relate this to Fig. 4.3, the upper signal corresponds to the positive polarity (hence $\hat{y}_+$), the middle corresponds to the zero polarity ($\hat{y}_0$) and the lower corresponds to the negative polarity ($\hat{y}\_$). The NPD is included in the figure, and one can see that $\tau_+ < 0$ and $\tau_- > 0$ relative the zero polarity signal.

In back-scatter imaging situations, an object is observed at a narrow region around the beam axis. In such situations, the HF propagation delay may be approximated as

$$t(z) = \int_{\Gamma(z)} \frac{ds}{c(s,p_{LF}(s))} = t_0(z) + \tau(z) \tag{4.3}$$

where $\Gamma(z)$ is the transmit beam axis of the HF pulse to a scatter at depth z. The coordinate s corresponds to the ray location of the HF pulse at any time. The propagation delay without any LF manipulation is then

$$t_0(z) = \int_{\Gamma(z)} \frac{ds}{c_0(s)}$$

and the added first order nonlinear propagation delay (NPD) at the center of gravity of the HF pulse due to presence of LF manipulation pressure is

$$\tau(z) = -\int_{\Gamma(z)} \frac{ds}{c_0(s)} \beta(s) p_{LF}(s) \tag{4.4}$$

For a plane wave ds = dz and $\Gamma(z)$ = [0, z] (Hansen et al. 2011). One can see that the $|\tau|$ will increase as long as $p_{LF} > 0$, which is assumed to be true during forward propagation in soft tissues because $p_{LF} \approx 0$ after being scattered by a diffusive domain.

From Eq. (4.4) it is indicated that $\beta(z)$ can be obtained from $\tau(z)$ by differentiation. Unfortunately, this does not yield sufficient estimates of $\beta(z)$ due to noise in measurements of the NPD. An alternative method to find $\beta(z)$ has been published by Kvam et al. (2019), and will be presented in the following section.

4.2.1 Estimation of NEP

An estimate of the NEP can be calculated using the SURF method presented by published by Kvam et al. (2019). This is a model-based fitting approach where the NPD is both measured and modeled to formulate an optimization problem for estimating the NEP.

The following ideas are used in the SURF method:

- A LF field is modeled to calculate the modeled NPD τ_x.

- A limitation of possible β values, such that $\beta \in [\beta_{\text{min}}, \beta_{\text{max}}]$. As an example, typical values of β are 1-4 GPa^{-1} in soft tissues.
- The measured NPD τ_{y} is composed of both noise and signal, and in general $\tau_{\text{n}} \leq \tau_{\text{y}} \leq \tau_{\text{x}}$, where τ_{n} describe the noise delay.
- Plane wave propagation.

Based on these ideas an estimation functional (EF) is defined and minimized to estimate $\beta(\text{z})$. Before presenting the EF, necessary parts of the optimization problem will be presented.

Measuring NPD

The measured NPD, $\tau_{\text{y}}(\text{t})$, is simply a measurement of the delay between two signals. The following method uses the phase shift between the signals and derivation is derived in Brende (2015).

Two analytic signals will be considered, one nonzero-polarity pulse and one zero-polarity pulse. The zero-polarity pulse is given by

$$\text{y}_0(\text{t}) = \text{a}(\text{t})\text{e}^{i\omega_{\text{c}}\cdot\text{t}+i\phi(\text{t})}$$

where ω_{c} is the center frequency of the HF pulse, a(t) is the amplitude, and $\phi(\text{t})$ is the phase.

The nonzero-polarity pulse will have a delay τ_{y} relative $\text{y}_0(\text{t})$, such that it can be represented by

$$\text{y}_{\text{p}}(\text{t}) = \text{a}(\text{t}-\tau_{\text{y}})\text{e}^{i\omega_{\text{c}}\cdot(\text{t}-\tau_{\text{y}})+i\phi(\text{t}-\tau_{\text{y}})}$$

where p denotes the polarity (being + or -).

The delay between $\text{y}_0(\text{t})$ and $\text{y}_{\text{p}}(\text{t})$ can be estimated by computing the phase shift between them, as

$$\begin{aligned}
\angle\{\text{y}_0(\text{t})\text{y}_{\text{p}}^*(\text{t})\} &= \angle\{\text{a}(\text{t})\text{a}(\text{t}-\tau_{\text{y}})\text{e}^{i\omega_{\text{c}}\cdot(\text{t})+i\phi(\text{t})}\text{e}^{-i\omega_{\text{c}}\cdot(\text{t}-\tau_{\text{y}})-i\phi(\text{t}-\tau_{\text{y}})}\} \\
&= \omega_{\text{c}}\cdot\text{t} + \phi(\text{t}) - \omega_{\text{c}}\cdot(\text{t}-\tau_{\text{y}}) - \phi(\text{t}-\tau_{\text{y}}) \\
&= \omega_{\text{c}}\cdot\tau_{\text{y}} + \phi(\text{t}) - \phi(\text{t}-\tau_{\text{y}}) \\
&= \tau_{\text{y}}\Big[\omega_{\text{c}} + \dot{\phi}(\text{t}-\tau_{\text{y}}/2)\Big]
\end{aligned} \tag{4.5}$$

where the definition of derivative is used in the last step. Here one can explicitly see that the phase difference is proportional to the delay τ_{y}.

The signals $y_0(t)$ and $y_p(t)$ will also obtain a change in phase over an interval [t-δ_t, t+δ_t]. By averaging these phase differences, the delay between the signals can be estimated. First, the change in phase for $y_0(t)$ becomes

$$\begin{aligned}\angle\{y_0(t+\delta_t)y_0^*(t-\delta_t)\} &= \omega_c \cdot (t+\delta_t) + \phi(t+\delta_t) - \omega_c \cdot (t-\delta_t) - \phi(t-\delta_t) \\ &= 2\omega_c\delta_t + \phi(t+\delta_t) - \phi(t-\delta_t) \\ &= 2\omega_c\delta_t + 2\delta_t\dot{\phi}(t) \\ &= 2\delta_t\Big[\omega_c + \dot{\phi}(t)\Big]\end{aligned}$$

Similarly, the change in phase for $y_p(t)$ becomes

$$\begin{aligned}\angle\{y_p(t+\delta_t)y_p^*(t-\delta_t)\} &= \omega_c \cdot (t-\tau_y+\delta_t) + \phi(t-\tau_y+\delta_t) \\ &\quad - \omega_c \cdot (t-\tau_y-\delta_t) - \phi(t-\tau_y-\delta_t) \\ &= 2\delta_t\Big[\omega_c + \dot{\phi}(t-\tau_y)\Big]\end{aligned}$$

The average phase difference for each time step δ_t can then be used to estimate the delay τ_y in Eq. (4.5) as follows

$$\frac{1}{2\cdot 2\delta_t}\left(2\delta_t\Big[\omega_c + \dot{\phi}(t)\Big] + 2\delta_t\Big[\omega_c + \dot{\phi}(t-\tau_y)\Big]\right) \approx \omega_c + \dot{\phi}(t-\tau_y/2)$$

or equally

$$\frac{1}{4\delta_t}\left(\angle\{y_0(t+\delta_t)y_0^*(t-\delta_t)\} + \angle\{y_p(t+\delta_t)y_p^*(t-\delta_t)\}\right) \approx \frac{1}{\tau_y}\angle\{y_0(t)y_p^*(t)\}$$

Hence,

$$\tau_y(t) \approx \frac{4\delta_t\angle\{y_0(t)y_p^*(t)\}}{\angle\{y_0(t+\delta_t)y_0^*(t-\delta_t)\} + \angle\{y_p(t+\delta_t)y_p^*(t-\delta_t)\}}$$

LF field

The optimization problem of estimating the NEP requires knowledge about the LF field. For *in vitro* measurements the LF field is unknown, such that a modeled LF field is used instead. The modeled approximation is made by hydrophone measurements of the LF field in a water tank and details about the model are available in Kvam et al. (2019).

The LF pressure used in the estimation of the NEP is shown in Fig. 4.4. At x ≈ -7.5 mm there are broken transducer elements in the probe which is the reason for the low LF field.

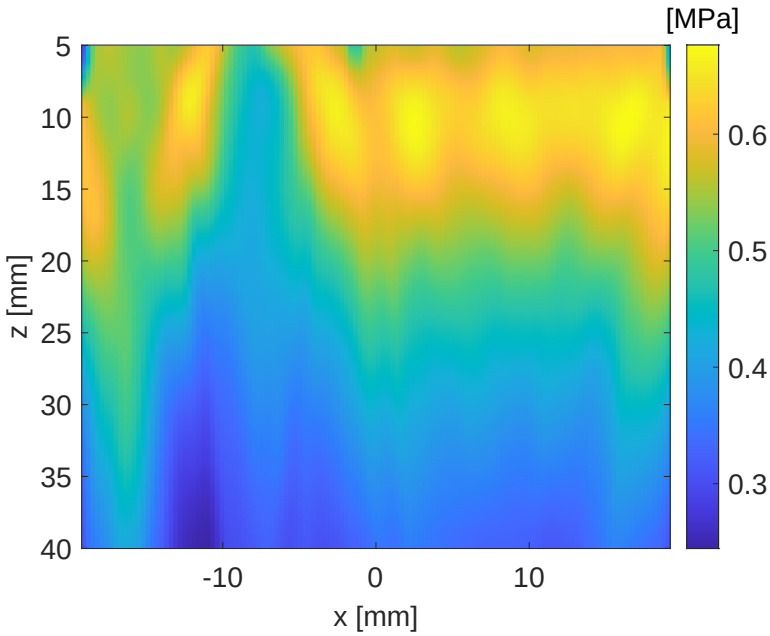

Figure 4.4: LF field used to calculate the modeled NPD.

The LF beam is designed such that the phase shift of the LF pulse across the imaging region is minimal. This leads to an accumulative modeled NPD τ_x as the sign of the LF pressure experienced by the HF pulse is constant. This can also be observed in Eq. (4.4).

Modeling NPD

The modeled NPD $\tau_x(t)$ is calculated by integration over time rather than depth as in Eq. (4.4). In this way c_0 is eliminated from the equation since time $t = 2z/c_0$. The substitution becomes $du/ds = 2/c_0$ for u and s being the integration variable in time and depth, respectively. This gives

$$\tau_x(t) = -\int_0^t \frac{\beta(u) p_{LF}(u)}{2} du \tag{4.6}$$

Estimation functional

The optimization problem of estimating the NEP is solved by finding the β parameters which minimize the EF. The EF is a sum of a distance term and a regularization term defined as

$$\mathrm{H}[\beta(\mathrm{z})] = \int_{\mathrm{z}} \mathrm{dz} \left\{ \mathrm{W_D}(\mathrm{z}) \left[\frac{\tau_{\mathrm{y}}(\mathrm{z}) - \tau_{\mathrm{x}}(\mathrm{z})}{\tau_{\mathrm{x}}(\mathrm{z})} \right]^2 + \mathrm{W_R}(\mathrm{z}) \left| \nabla \beta(\mathrm{z}) \right| \right\} \tag{4.7}$$

for

$$\beta_{\min} < \beta < \beta_{\max}$$

where $\beta_{\min}$ and $\beta_{\max}$ is the limitation of the solution space.

$\mathrm{W_D}$ is a distance weight which controls the penalty for deviation between τ_{y} and τ_{x}. $\mathrm{W_D}$ is set to a high value in areas where the probability is high for a good estimate of the NEP.

$\mathrm{W_R}$ is a regularization weight defined as 1-$\mathrm{W_D}$. In this way, the weight relaxes the smoothness criteria in regions where a gradient shift is expected.

The weights adjust the amount of contribution of each term to the EF depending on the circumstances and are designed in three different ways which will be described in Section 5.4.

To decrease the number of parameters in the optimization problem, the scan line is divided into sub-intervals. The estimated parameters are upsampled to the original frequency using linear interpolation.

Each scan line in the ultrasound image is estimated individually, but a lateral filter is applied to the result. Each scan angle is also optimized individually and averaged afterward.

The method of moving asymptotes from the NLopt library implemented by Svanberg is used as a solver to the optimization problem.

Chapter 5

Method

More than 100 GB of data was collected for this thesis. In this chapter, an insight into how the data was measured will be given. This includes a brief introduction to the scanner used, a description of the experimental setup and details about the measurements which may be interesting for reproducing the experiments. In the end, three different versions of the distance weight used to process the data are presented.

5.1 Verasonics Vantage Research System

The Verasonics Vantage Research System is a complex tool for transmitting, receiving and process ultrasound information. The system consists of a data acquisition hardware and a host controller computer. The host controller computer can be programmed by the user which makes the Verasonics a powerful tool for ultrasound experiments, as nearly all thinkable parameters can be chosen by the user.

For the dual frequency ultrasound experiments, the Verasonics Vantage Research System was used. A linear dual frequency probe of 128 HF elements and 52 LF elements was used to do measurements pulse-echo acquisition, which allows in vitro studies. By transmitting multiple pulse complexes with varying LF polarity, the nonlinear propagation of material can be studied. The LF wave is an unfocused plane wave to obtain a homogeneous LF pressure, with an aperture of 46.8 mm and a frequency of 0.8 MHz. The HF wave has a 30 mm focal length with an aperture of 6 mm, which gives the f-number 30 mm / 6 mm = 5. The big f-number is important in the SURF method to avoid a sharp focus. The frequency of the HF wave is 8 MHz. Both the HF and the LF wave have steering angles -4°, 0°and 4°at

30 volts.

5.2 Experimental setup

Fig. 5.1 shows an illustration of the experimental setup. In the figure, one can see a stand (A) keeping the ultrasound probe (B) stable during measurements. The probe is pointed to the object to be imaged[1] (E), which is kept in a box (D) filled with a liquid (C). In the bottom of the box, an absorbing mat (F) is placed to avoid reflection of the ultrasound waves which have not been reflected before reaching the bottom. The height of the probe can be adjusted.

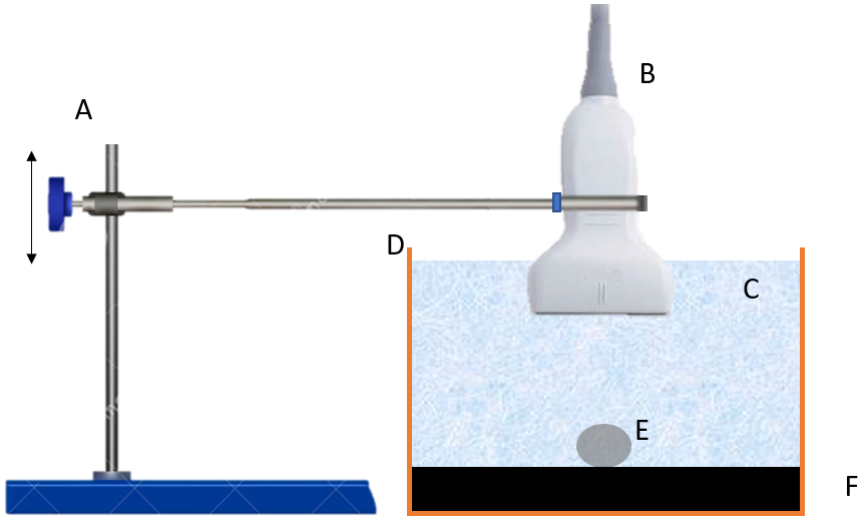

Figure 5.1: Illustration of experimental setup

5.3 Experiments

40 experiments were carried out. Healthy tissue was measured for comparison with literature values, but the main goal was to study tumors. Details from all measurements are given in Table 5.1 and Table 5.2, and pictures from one measurement are shown in Fig. 5.2 and Fig. 5.3.

All tumors were pancreatic ductal adenocarcinoma (PDAC) tumors originating from KPC mice. KPC is short for K-Ras, p53, and Cre. Kras is a gene responsible for making the protein Kras, which takes part in the RAS/MAPK pathway [2]. p53 is a gene that plays a role in controlling cell division and cell death. Cre is an enzyme used to carry out site-specific recombination events in the Deoxyribonucleic

[1] Here: tumor or organ

[2] Signaling pathway important for cell proliferation, differentiation and death

Figure 5.2: Experimental setup. The transducer is kept stable approximately 20 mm above center of the object to be imaged. Here tumor F is placed in the NaCl solution at 23 °C ready to be measured.

Acid (DNA). For KPC mice, Cre is used to activate Kras and p53 in the mouse pancreas, which leads to the development of pancreatic cancer. [3]

The experiments typically consisted of receiving the object[4] kept in a tube. A received tumor is shown in Fig. 5.4. The object was then kept in a NaCl 9 mg/ml solution until a specific temperature was assumed to be reached. Fig. 5.5 shows the organs of mouse MX being tempered. The time to temper was approximated using Newton's law of heating.

[3] In most cases, Kras and p53 do not cause cancer spontaneously when they are activated. Cancer is, as mentioned in Section 2.1, uncontrolled cell differentiation which may occur if there are mutations in Kras and p53.

[4] "the object" refers to the healthy tissue or the tumor, i.e. the object to be measured

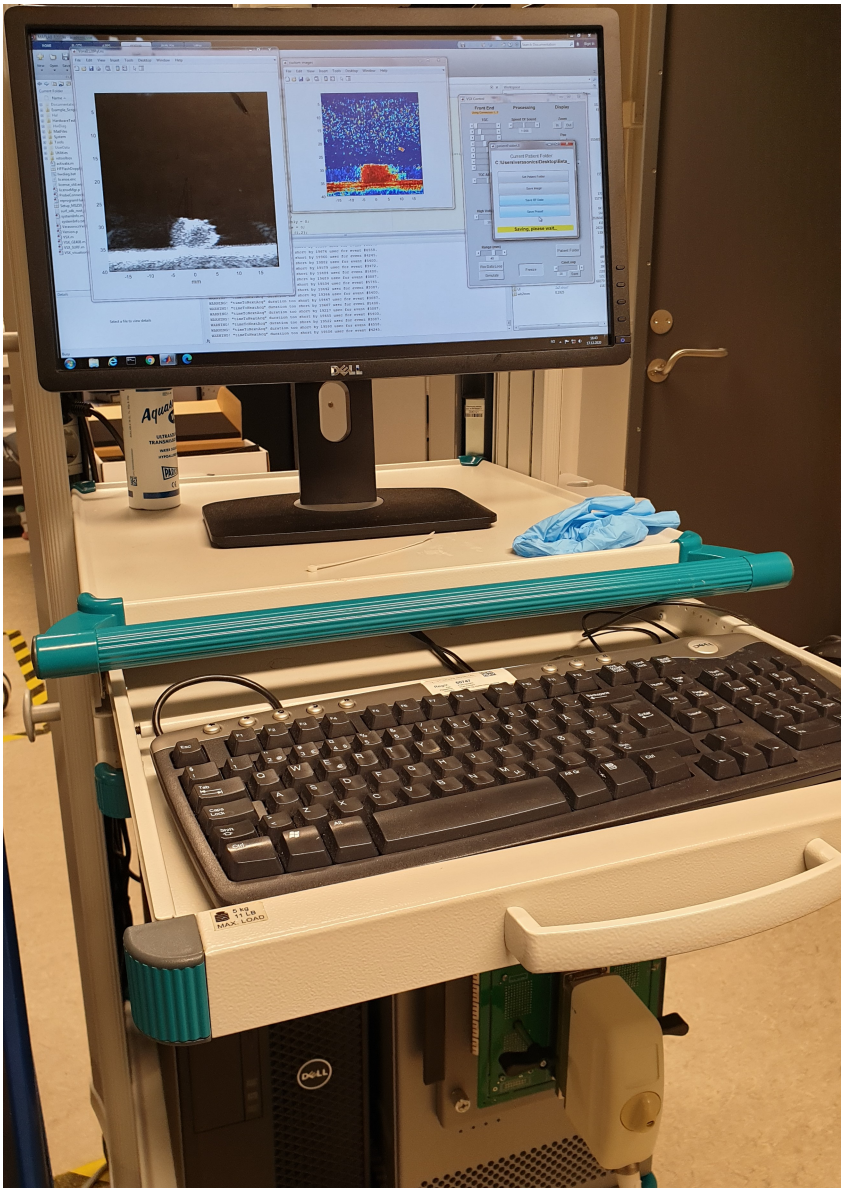

Figure 5.3: Display during experiment. The image to the left is the conventional B mode image, while the image to the right is the measured NPD.

Table 5.1: Details of experiments made on tumors. PDAC is short for pancreatic ductal adenocarcinoma. The label "-s" refers to "slice" which means another layer of the tumor.

Tumor/ mouse	Date	Cancer type	Frozen	Temperature [°C]	Depth [mm]
A	17.12.20	PDAC	1	-	16
A	17.12.20	PDAC	1	-	34
A	17.12.20	PDAC	1	-	19
B	10.02.21	PDAC	1	20	20
B	10.02.21	PDAC	1	34	20
Bb	10.02.21	PDAC	1	34	20
B	16.02.21	PDAC	2	23	17
B	16.02.21	PDAC	2	34	17
C	16.02.21	PDAC	0	23	20
C	16.02.21	PDAC	0	37	15
C	24.02.21	PDAC	1	22	20
C	24.02.21	PDAC	1	33	20
C,D	16.02.21	PDAC	0	23	20
D	16.02.21	PDAC	0	23	20
D	16.02.21	PDAC	0	35	17
D	24.02.21	PDAC	1	22	20
D	24.02.21	PDAC	1	34	20
E	24.02.21	PDAC	0	22	20
E-s	24.02.21	PDAC	0	22	20
E	24.02.21	PDAC	0	35	20
F	24.02.21	PDAC	0	22	20
F	24.02.21	PDAC	0	38	20
E	23.03.21	PDAC	1	23	18
E-s	23.03.21	PDAC	1	23	18

Table 5.2: Details of experiments made on mouse organs. The kidneys are labeled 1 and 2 to show that measurements originate from different organs. The label "-s" rand "-ss" refers to "slice" which means another layer of the organ.

Mouse	Date	Tissue	Frozen	Temperature [°C]	Depth [mm]
MX	16.03.21	brain	0	23	22
MX	16.03.21	brain	0	36	18
MX	16.03.21	kidney (1)	0	23	22
MX	16.03.21	kidney (1)	0	35	20
MX	16.03.21	kidney (2)	0	23	22
MX	16.03.21	kidney (2)	0	33	20
MX	16.03.21	liver	0	23	22
MX	16.03.21	liver	0	38	20
MX	16.03.21	muscle, skeletal	0	23	22
MX	16.03.21	muscle, skeletal	0	32	20
MX	23.03.21	liver	1	23	18
MX	23.03.21	liver	1	23	18
MX	23.03.21	liver	1	23	18
MY	16.03.21	kidney (1)	0	23	20
MY	16.03.21	kidney (1)	0	35	20
MY	16.03.21	kidney (2)	0	23	20
MY	16.03.21	kidney (2)	0	36	20
MY	16.03.21	liver	0	23	20
MY	16.03.21	liver	0	34	20
MY	16.03.21	muscle, skeletal	0	23	20
MY	16.03.21	muscle, skeletal	0	32	20
MY	23.03.21	kidney	1	23	18
MY	23.03.21	kidney-s	1	23	18
MY	23.03.21	liver	1	23	18
MY	23.03.21	liver-s	1	23	18
MY	23.03.21	liver-ss	1	23	18

Figure 5.4: Tumor A received for measurements. The diameter of the tumor is approximately 8 mm.

Figure 5.5: Organs of mouse MX. The biggest organ is the liver (approximately 1 cm x 1 cm in size). The rest of the organs are, from left to right, kidney, kidney, skeletal muscle and brain.

5.3.1 Newtons law of heating

Newtons law of heating is given by

$$\frac{dT}{dt} = k(T\text{-}T_s)$$

where T is the temperature of the tumor, T_s is the temperature of the surroundings, t is the time and k is a constant. The temperature T as a function of time can be found by solving the differential equation

$$T(t) = T_s + (T_0 - T_s)e^{kt} \tag{5.1}$$

where T_0 is the initial temperature of the tumor.

The constant k varies with the size, the specific heat capacity c_p, the heat transfer coefficient h and the density ρ of the object to be heated, in addition to the contact area M between the surroundings and object.

$$k = \frac{hM}{mc_p} \tag{5.2}$$

A rough estimate of k will be used as the goal only is to ensure tempering of the tumor. First, the tumors are assumed to be spherical with a radius r =0.5 cm. This means that Eq. (5.2) can be rewritten to

$$k = \frac{3h}{r\rho c_p}$$

The density and specific heat capacity is set to $\rho = 920\ \text{kg/m}^3$ and $c_p = 3600$ J/kg°C, respectively, based on literature (Hassan et al. 2009).

An equivalent heat transfer coefficient between tissue and blood in a porous model has been investigated by Yuan. The result varied between 100 $\text{W/m}^{2\circ}\text{C}$ and 300 $\text{W/m}^{2\circ}\text{C}$. The tissue and blood have been assumed to be comparable to the tumor and liquid, but h is chosen to be below the lower value to ensure the tempering time to be big enough. All parameters necessary for Newton's law of heating are calculated and given in Table 5.3.

Typically, the tumors are kept in the freezer at -80 °C or at room temperature. Newton's heating curve for these two cases is shown in Fig. 5.6, where one can see that it takes about 5 minutes to temper the tumors when they are kept in a NaCl solution. Again, this is a rough estimate just to get a feeling of the time, details are not important.

Table 5.3: Parameters for Newtons law of heating

Parameter	Value	Unit	Description
ρ	920	kg/m^3	Density
c_p	3600	J/kg°C	Specific heat capacity
r	0.5	cm	Radius
h	80	W/m^2°C	Heat transfer coefficient
k	0.014	s^{-1}	Constant in Eq. (5.1)

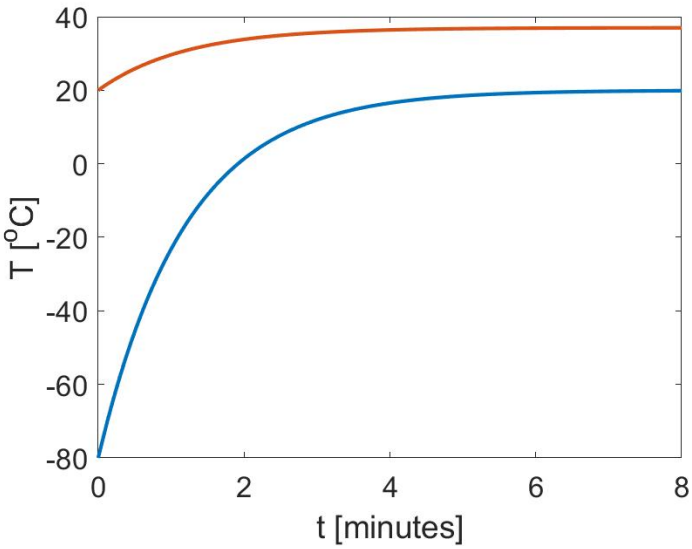

Figure 5.6: Newton's heating law for tumors in a NaCl solution as a function of time. The orange curve shows room tempered tumors heated to body temperature, while the blue curve shows tumors kept in the freezer heated to room temperature.

5.4 Code versions

Three different versions were tested and compared. It is the weights in the estimation functional (EF) (given in Eq. (4.7)) which are different for the three version, and the additional code has been provided by Surf Technology. The functional is a weighted sum of a distance term and a regularization term, where the weights in many ways tell how much we trust the measured delay at a given point. If the distance weight W_D is low, the delay model will be made based on surrounding data, while for a high W_D the delay model will be based on nearby data.

The regularization weight W_R and W_D sum to one, which makes the calculation of W_R easy.

Below the distance weights in the different versions are described.

5.4.1 Version 1

Version 1 was, as the name implies, the first version to be made. The distance weight is a product of three contributions:

w1: Strong scatters are higher weighted. By applying a high pass filter to the received zero polarity RF data, the local strong scatters will deviate from surrounding diffusive scattering. This gives

$$w1 = \frac{env_0 \circledast h_{T1\lambda}}{(env_0 \circledast h_{T4\lambda})^3}$$

where env_0 is the envelope of the received zero polarity RF data, and $h_{T1\lambda}$ and $h_{T4\lambda}$ are impulse responses of averaging low pass filters for one and four wavelengths, respectively. The ratio between he low pass filters acts like high pass filter. The weight is normalized such that values are between 0 and 1.

w2: Areas with a sudden drop in the measured NPD in areas we assume to be homogeneous[5] is a typical sign of artefacts. As a consequence, non-homogeneous areas horizontally in the measured delay are set to have a lower weight. The weight is based on homogeneity horizontally as the measured NPD increase with depths.

The weight is found by filtering the measured NPD τ_y using median filter with small filter height and a big filter width [6]. This gives a filtered measured NPD $\tilde{\tau_y}$. The difference between the measured NPD and the filtered

[5] E.g inside the tumor

[6] Small means approximately 1/10 of object height, while big means approximately 1/2 of object width

measured NPD $\Delta\tau_y = |\tau_y - \tilde{\tau_y}|$ will therefore disclose artefacts, such that the weight is chosen to be

$$w2 = 1 - \Delta\hat{\tau_y}$$

where $\Delta\hat{\tau_y}$ means $\Delta\tau_y$ normalized. The weight is hence high in homogeneous areas and low in non-homogeneous areas and has values between 0 and 1.

w3: Segmentation of the object based on a combination between a horizontal and a vertical segmentation.

The horizontal segmentation is found by locating the bottom and mask the area correspondingly the object diameter above the bottom. The diameter is set to be 8mm for tumors and between 4mm and 10mm for organs depending on the size. The bottom is a very strong reflector and hence easy to locate.

The vertical segmentation is based on the sum of signal strength vertically inside the object. The objects are assumed to be spherical shaped, such that the sum of the vertical signal will be maximum in the center of the object. The mask is therefore the vertical area corresponding to the radius of the object to each side from the center.

By multiplying the horizontal and vertical segmentation, a mask for the object can be found. This contribution is either 0 or 1.

This gives W_D = w1*w2*w3.

5.4.2 Version 2

Version 2 is a modification of version 1. Only the segmentation of the object is adjusted, such that the distance weight is still a product of three contributions, where w1 and w2 are unchanged from version 1. w3 is modified to:

w3: Segmentation of the object based on signal strength (as water does not scatter) and size of measured NPD (larger delay inside than outside object). Both thresholds are found experimentally. Everything below the bottom is removed. To ensure no disturbing signals from the bottom, 1mm above the located bottom is also removed. Furthermore, the object in the box is segmented based on signal strength, as the surrounding water does not scatter.

This gives similarly W_D = w1*w2*w3, where w1 and w2 are described in Section 5.4.1.

5.4.3 Version 3

Version 3 is a modification of version 2. One additional contribution is added, and the weights are adjusted during the estimation of β.

The adjustment is based on an unexpected low modeled delay which leads to an inadequate estimation of β (details are discussed in Section 7.2). The distance weight is set to zero if the measured NPD is lower than the modeled NPD after one iteration in the solver. The relative error is chosen to be 5%, such that the condition for setting W_D to zero is given by

$$\frac{\tau_y - \tau_x}{\tau_x} < -0.05$$

The estimation of β is made again with the modified weight. This method requires 40 iterations of estimation instead of 20 [7], but this is negligible as the execution time is only approximately 40 ms per iteration.

The additional contribution of the distance weight is:

w4: Signal strength inside the object should be above a threshold relative max signal strength. The threshold is found experimentally and should not be mixed with the signal strength threshold in w3. This is an additional segmentation as we trust strong scatters more. The values of w4 are 0 or 1.

This gives W_D = w1*w2*w3*w4, where w1 and w2 are described in Section 5.4.1, and w3 is described in 5.4.2.

[7] Four frames and five steering angles were used in these experiments

Chapter 6

Results

Measurements were made on tumors A-E, with varying temperatures and the number of times being frozen, as described in Section 5.3. To have a reference to the estimated β values, measurements were also made on healthy tissues (brain, kidney, liver and skeletal muscle) from two mice.

This chapter is divided into four sections. The first section shows some general results required to estimate β. This includes conventional B-mode images, delay images, weights used and comparison between RF signals from different polarities.

The second section shows selected results using weights from code version 1 introduced in Section 5.4.1. The selected results are the ones that indicate why another version is necessary.

The third section shows selected results using weights from code version 2 introduced in Section 5.4.2. Again, the results did not fulfill the expectations and the selected results show why.

The fourth and last section contains results using code version 3 introduced in Section 5.4.3. This is the final version where modifications are made based on results from versions 1 and 2. The estimated β is shown for all tumors and organs, in addition to a deeper insight into the result. This includes plots showing the consequence of the β value in varying surroundings and statistical computations for precision and accuracy of the method.

This chapter will be embossed with figures, while the discussion of the results will be covered in the next chapter.

6.1 Pre-results

To be able to estimate β, several parameters are necessary. In this section, the most important ones will be presented, in addition to results from the first measurement. These results are included in this section as they were used to optimize the method rather than being a part of the experimental results.

6.1.1 B-mode, delay and weights

The pre-results are relatively similar for all measurements and therefore only one measurement is presented. Details of the chosen measurement are given in Table 6.1.

Table 6.1: Details of experiment

Tumor	Frozen	Temperature [°C]	Steering angle [°]
B	1	20	4

The conventional B mode image obtained is shown in Fig. 6.1.

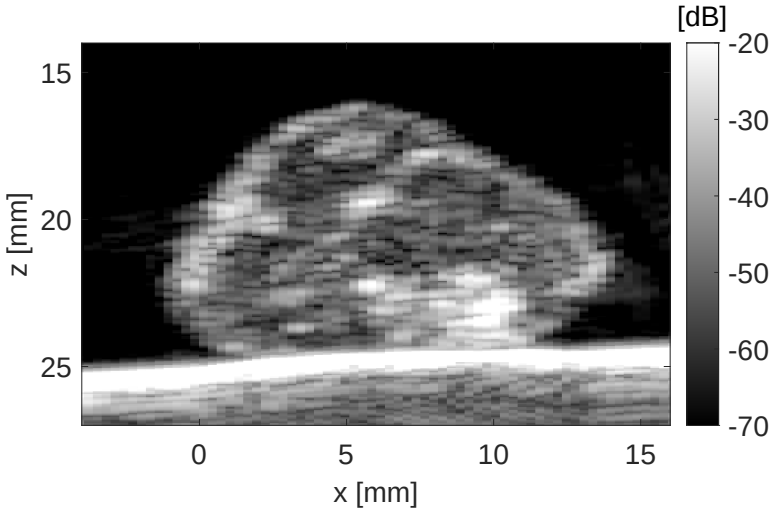

Figure 6.1: Conventional B mode of Tumor B. The B mode is used to calculate w1 as described in Section 5.4.1.

The RF signal for positive and negative polarity are shown for comparison in Fig. 6.2. The delay between these signals correspond to the delay image shown in Fig. 6.3.

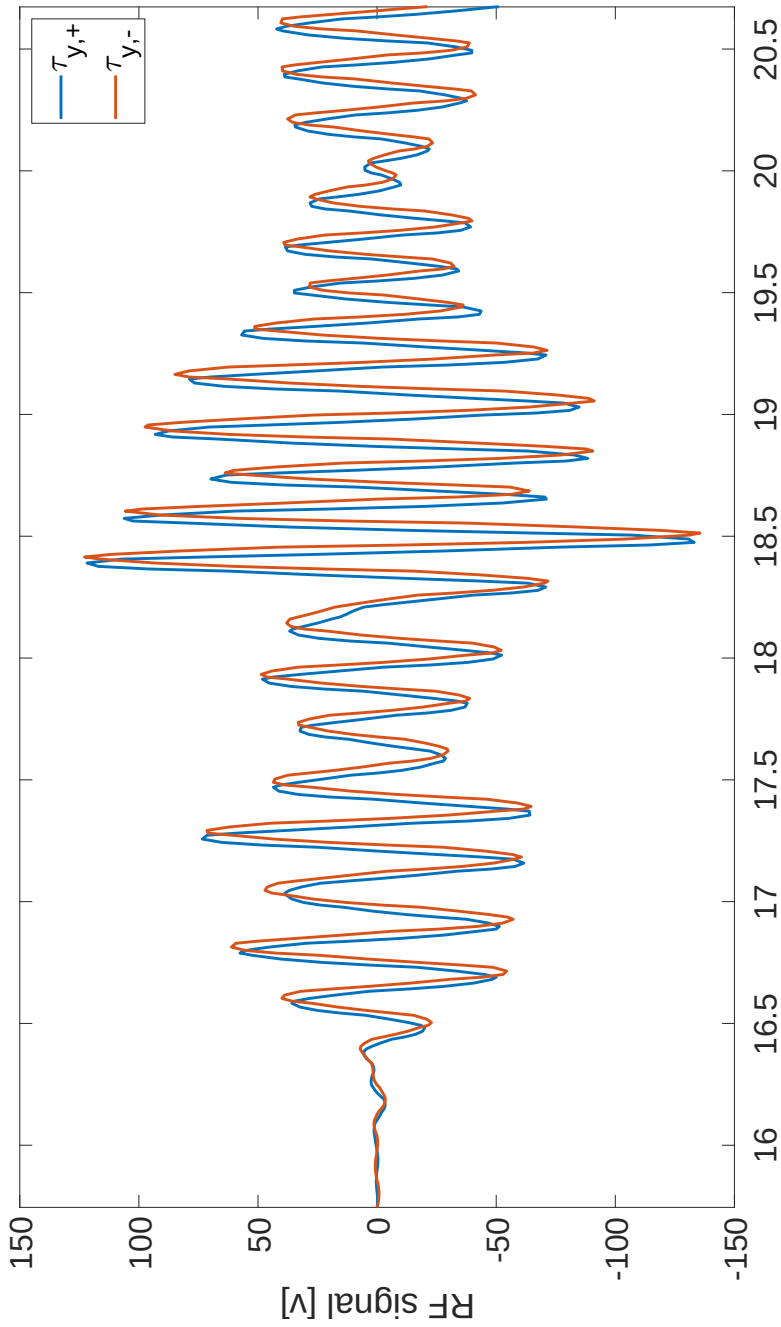

Figure 6.2: Comparison between measured delay with positive polarity ($\tau_{y,+}$) and negative polarity ($\tau_{y,-}$).

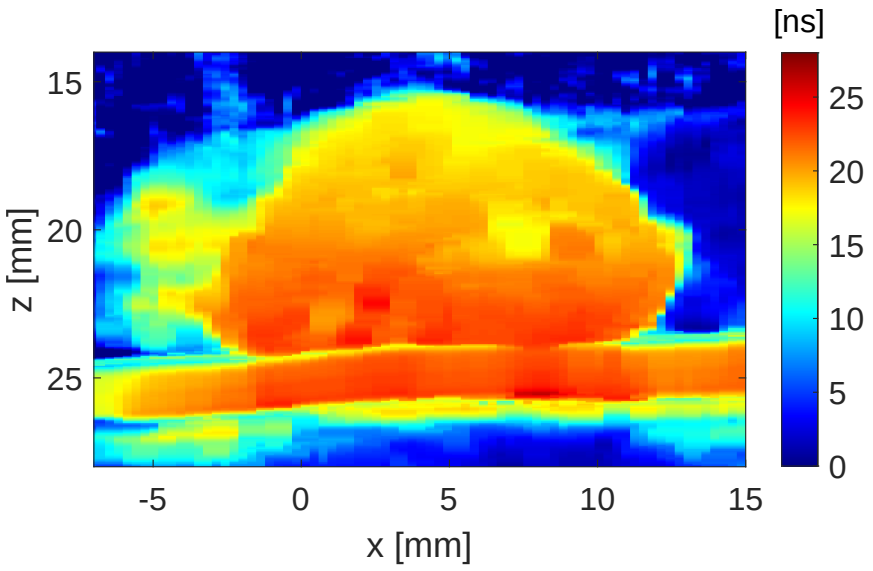

Figure 6.3: Measured NPD (τ_y)

The weights used to do the estimate of β for the different code versions are shown in Fig. 6.4.

6.1.2 Measurement used for optimization

The first measurement was made on tumor A in December and has been used to optimize the experimental method. The tumor had been frozen once, and measurements were taken at three different depths. Estimated β values are shown in Table 6.2.

6.2 Model with weights from version 1

The first version of code used to estimate β is described in section 5.4.1.

Results from the liver from mouse MY being fresh at 23 °C is used for presentation of code version 1. The segmentation showed to include parts of the bottom of the box in addition to not being suitable for non-spherical objects, which interfered the β estimation. The segmentation is shown in Fig. 6.5 and the estimated β values in the organ is shown in Fig. 6.6.

6.3 Model with weights from version 2

In this section certain results using weights from code version 2 described in 5.4.2 will be presented. The estimated β values showed to be inhomogeneous inside

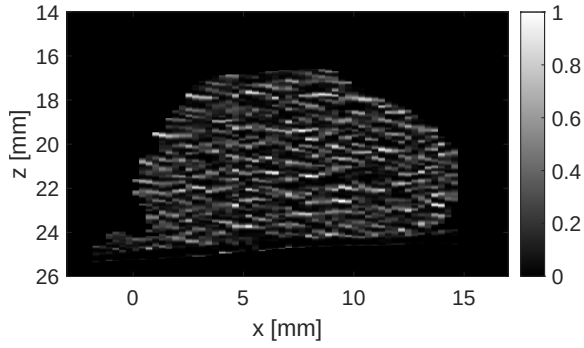

(a) Version 1

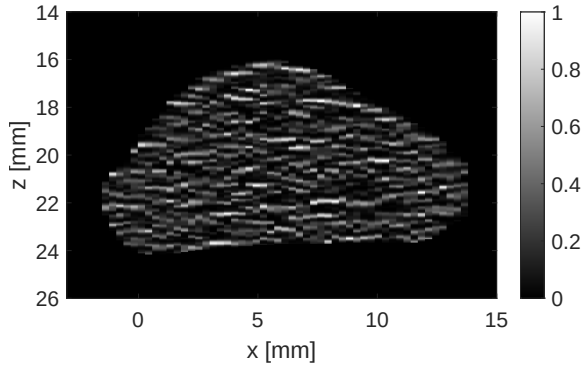

(b) Version 2

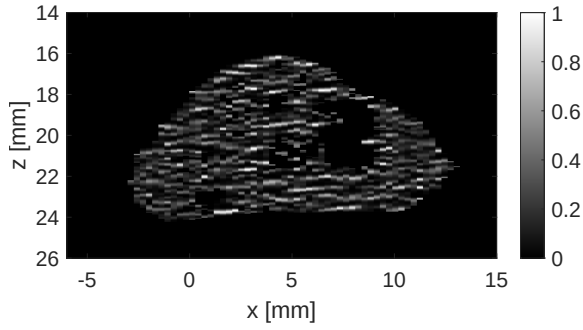

(c) Version 3

Figure 6.4: Weights used to estimate β for the three different code versions. Dark area means low weighting, brighter area means higher weighting.

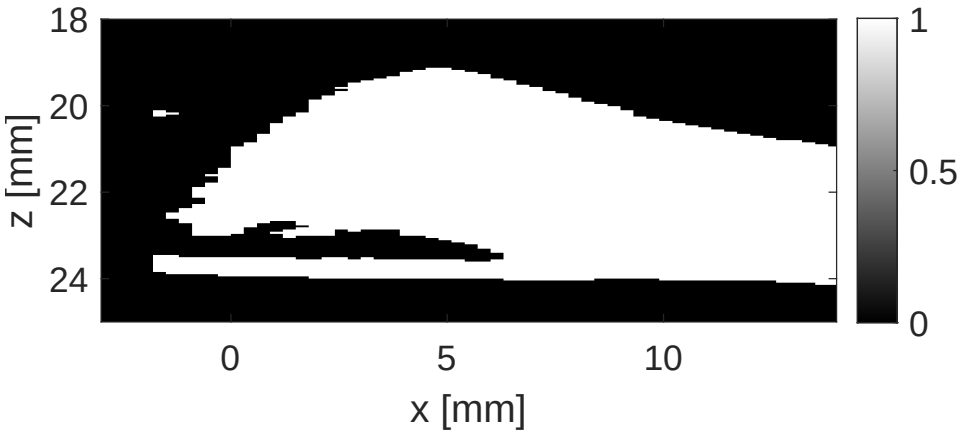

Figure 6.5: Segmentation of the liver of mouse MY using code version 1 introducd in Section 5.4.1. One can see that the bottom is included in the segmentation which acts as a disturbance in the estimation of β. The edges are sharp on the right side because of the big size of the liver.

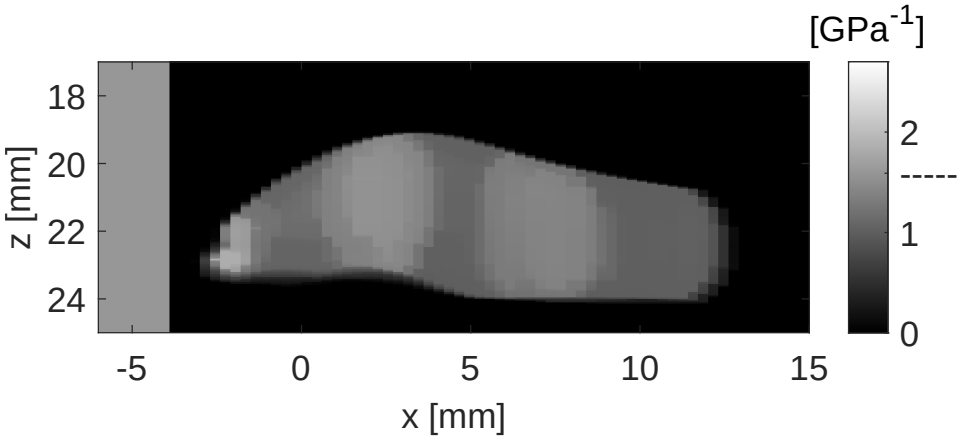

Figure 6.6: Values of β for the liver of mouse MY using code version 1. The gray area to the left in the figure correspond to the literature β value for liver and the marker on the color bar shows median value of the estimated β.

some of the tumors because of a sudden drop of the measured NPD.

Fig. 6.7 shows the estimated β values and the measured delay in the columns to the left. In the figure to the left, the modeled and measured delay through one scan line is plotted. The scan line is marked as a red line in the images to the left.

Fig. 6.8 shows the estimated β values for three tumors to show different occurrences of the inhomogenity.

Table 6.2: Tumor A

Depth	Frozen 1 time
16 mm	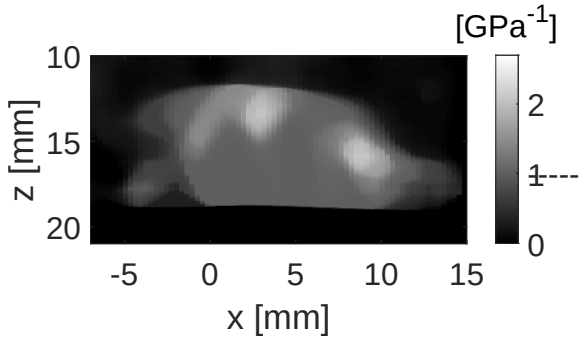
19 mm	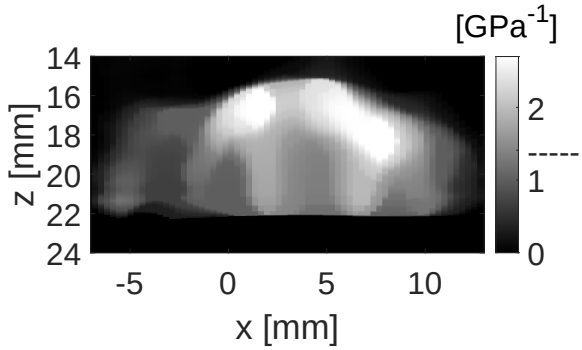
34 mm	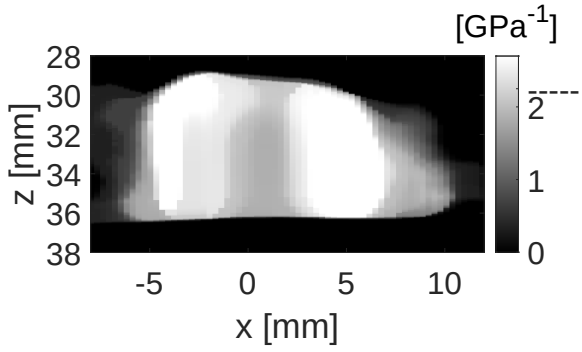

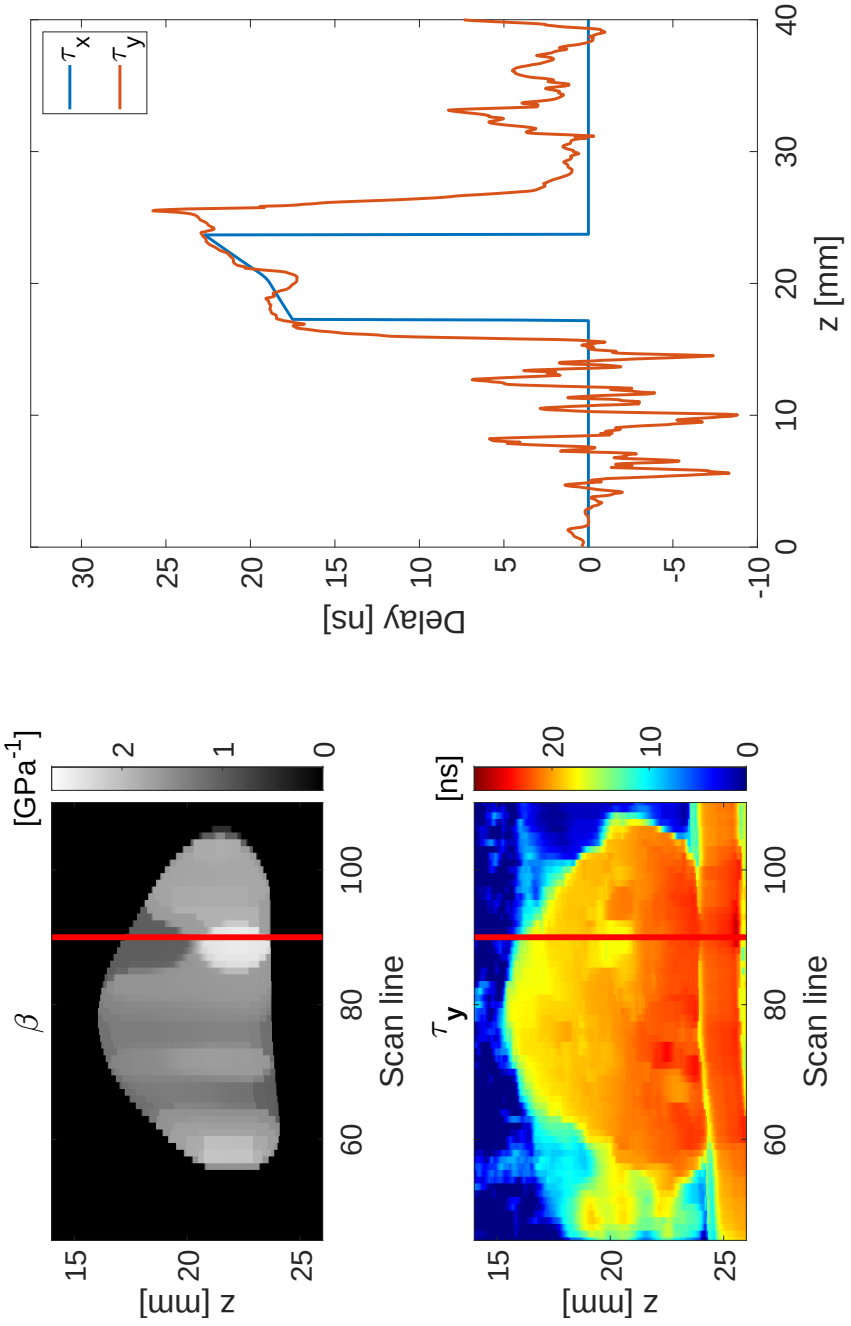

Figure 6.7: Estimated β values, measured NPD (τ_y) and modeled NPD (τ_x). The plot shows delay through one scan line (red line in images).

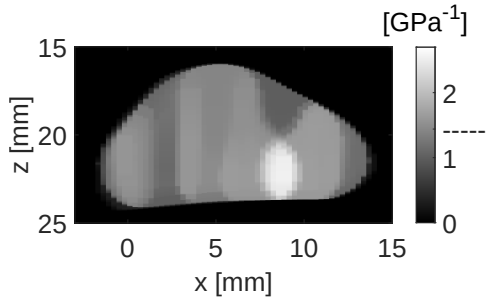

(a) Tumor B being frozen once at 20 °C.

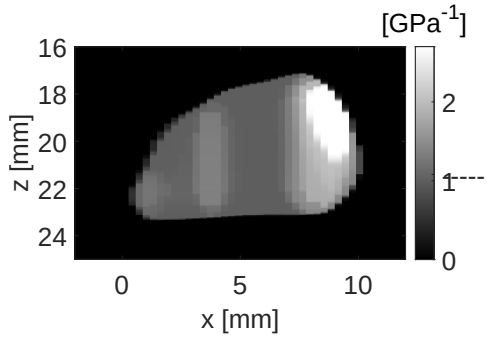

(b) Tumor D being frozen once at 34 °C.

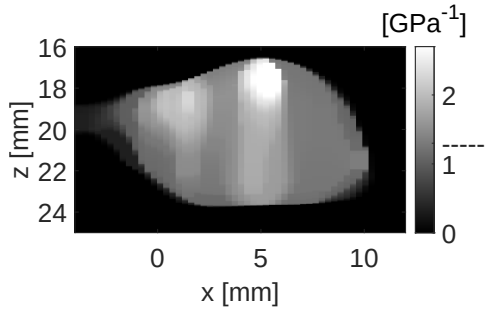

(c) Tumor F being fresh at 38 °C.

Figure 6.8: Estimated β values using weights from code version 2 described in Section 5.4.2. The bright areas is a consequence of unexpected drops in τ_y.

6.4 Model with weights from version 3

In this section results using weights from code version 3 described in section 5.4.3 will be presented. This is the final version of the code.

6.4.1 Estimated β values for tumors

In this section, the estimated β-values are presented for all tumors under varying circumstances (temperature and number of times being frozen).

A box plot summarizing the findings is shown in Fig. 6.9, and the average values for each of the cases shown in the box plot are given in Table 6.3.

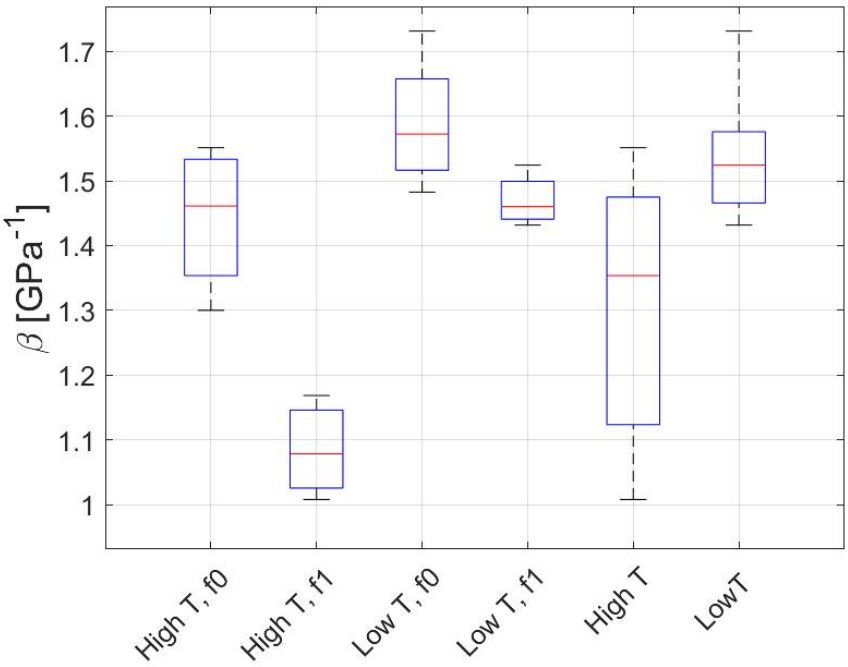

Figure 6.9: Box plot for estimated median β values of tumors. The red line indicates the median, and the bottom and top edges of the box indicate the 25th and 75th percentiles, respectively. The whiskers extend to the most extreme data points not considered outliers. Low T means temperatures between 20 °C and 23 °C, High T means temperatures between 33 °C and 38 °C, f0 means fresh tumors (frozen zero times) and f1 means that the tumors have been frozen once. In the two righter most cases, both f0 and f1 data are included.

There is one table with figures for each tumor, where temperature varies column-wise and the number of times being frozen and tempered varies row-wise. T low in the figures corresponds to room temperature (20-23°C), while T high corresponds

Table 6.3: Average estimated β values for tumor. Low T means temperatures between 20 °C and 23 °C and High T means temperatures between 33 °C and 38 °C. f0 means being fresh (frozen zero times) and f1 means being frozen once.

Case	$\beta[\text{GPa}^{-1}]$
T low, f0	1.59
T low, f1	1.47
T low	1.53
T high, f0	1.44
T high, f1	1.09
T high	1.31

to temperatures between 33°C and 38 °C, which is meant to correspond to body temperatures. The marker '—' on the color bar represents the median value of β.

Table 6.4: Tumor B

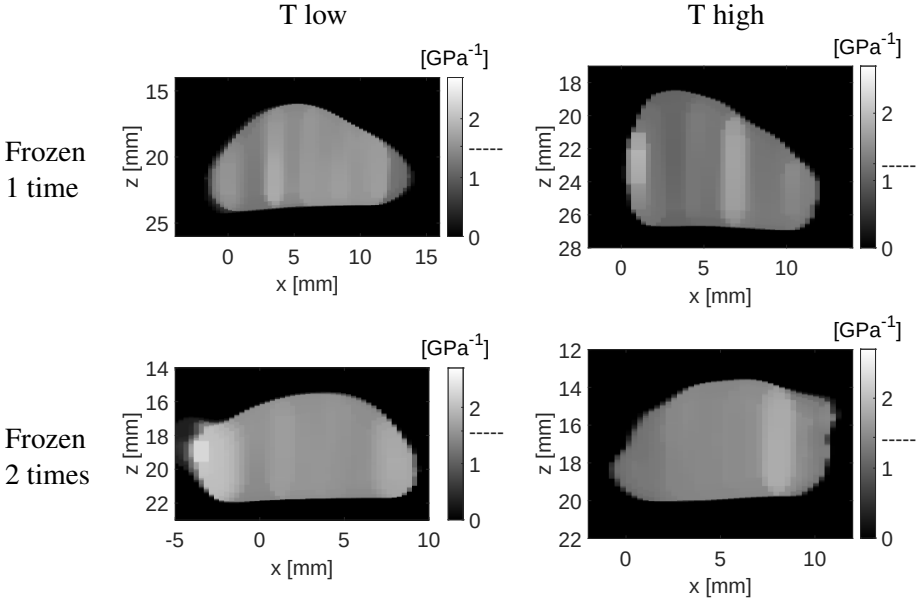

Table 6.5: Tumor C

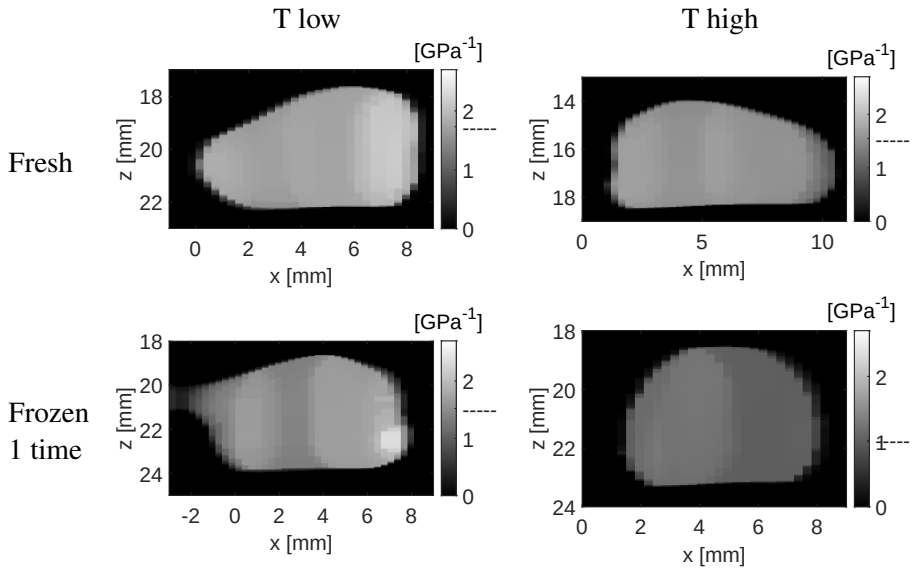

Table 6.6: Tumor D

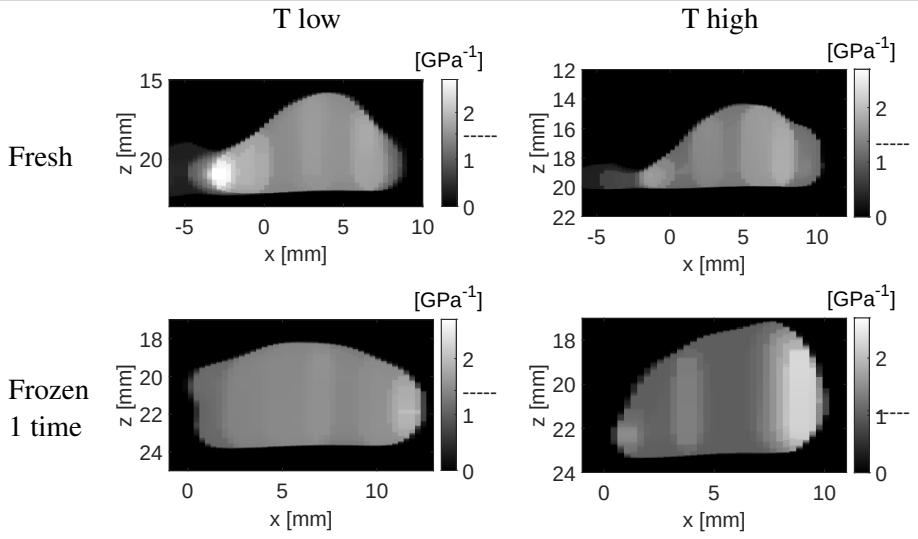

Table 6.7: Tumor E

	T low	T high
Fresh	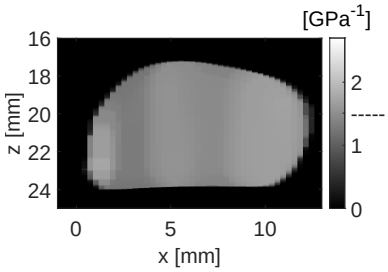	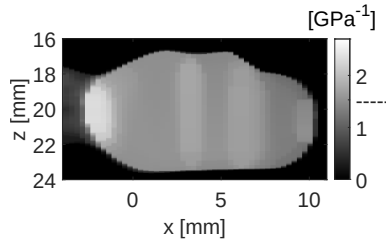
Fresh (other slice)	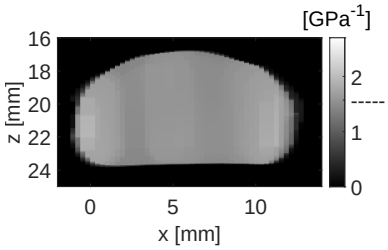	
	T low	T low (other slice)
Frozen 1 time	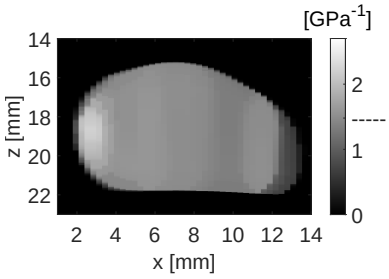	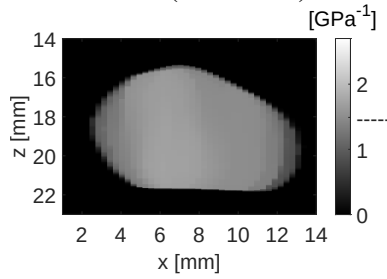

Table 6.8: Tumor F

	T low	T high
Fresh	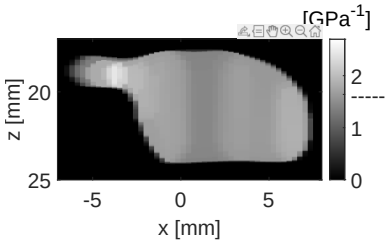	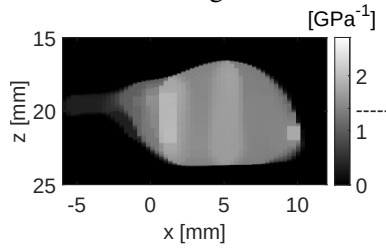

6.4.2 Healthy tissues as reference values

In this section estimated and literature β-values are presented for healthy tissues, using weights from code version 3 (described in Section 5.4.3).

Statistics

A summary of the findings is presented as a box plot in Fig. 6.10. The average β values are listed in Table 6.9 together with literature values for comparison[1]. The accuracy was calculated as the 100 - mean deviation [%] between estimated values and the literature values, and are given in Table 6.10.

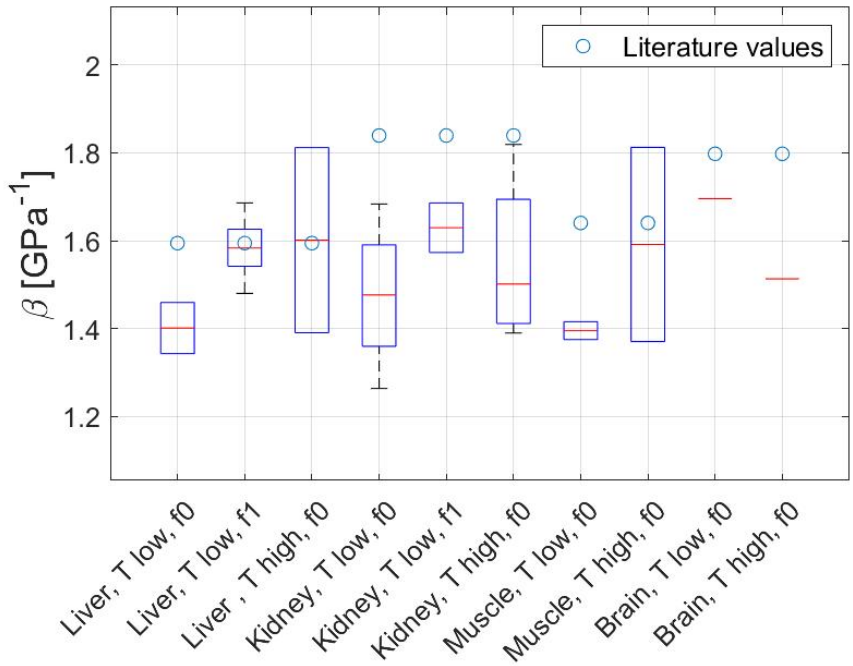

Figure 6.10: Box plot for estimated median β values of organs. The red line indicates the median, and the bottom and top edges of the box indicate the 25th and 75th percentiles, respectively. The whiskers extend to the most extreme data points not considered outliers. Low T means temperatures between 20 °C and 23 °C and High T means temperatures between 33 °C and 38 °C. f0 means being fresh (frozen zero times) and f1 means being frozen once. Data from organs being fresh and frozen once are included.

[1]The literature values originate from measurement made on humans, not mice, and are listed in Table 3.1.

Table 6.9: Average estimated and literature values of β for organs from mice. Low T means temperatures between 20 °C and 23 °C and High T means temperatures between 33 °C and 38 °C.

Case	Estimated β [GPa^{-1}]	Literature β [GPa^{-1}]
Liver, T high	1.60	1.59
Liver, T low	1.53	1.59
Kidney T high	1.55	1.84
Kidney, T low	1.53	1.84
Brain T high	1.51	1.80
Brain, T low	1.70	1.80
Muscle T high	1.59	1.64
Muscle, T low	1.40	1.64

Table 6.10: Accuracy at different temperatures and number of times being frozen. Low T means temperatures between 20 °C and 23 °C and High T means temperatures between 33 °C and 38 °C. f0 means being fresh (frozen zero times) and f1 means being frozen once.

Case	Accuracy [%]
T low, f0	87.0
T low, f1	93.9
T high, f0	91.2

Images

There is one table with figures for each organ from each of the two mice. The rows and columns in the tables are labeled and show a variety of temperatures, slices and the number of times being frozen. T low in the figures corresponds to room temperature (20-23°C), while T high corresponds to temperatures between 33 °C and 38 °C, which is meant to correspond to body temperatures.

In each figure there is a colored area to the left that corresponds to the literature β value for comparison with the experimental result. The marker '—' on the color bar represents the median value of β for the experimental result.

Table 6.11: Brain, mouse MX

	T low	T high
Fresh	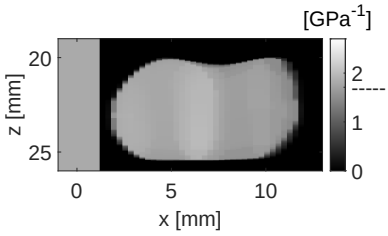	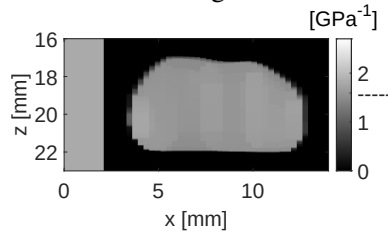

Table 6.12: Kidneys (one row for each kidney), mouse MX.

	T low	T high
Fresh	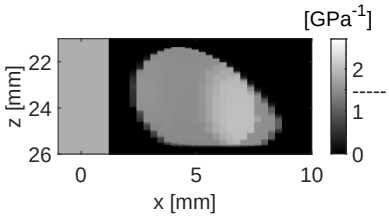	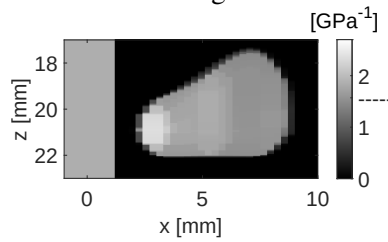
Fresh	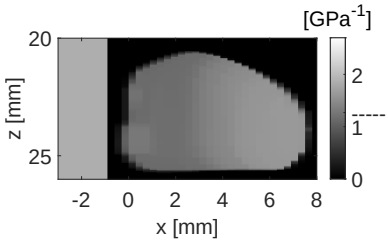	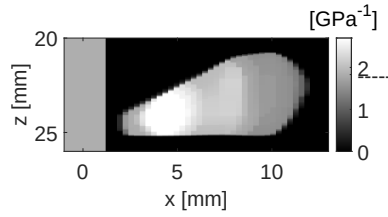

Table 6.13: Liver, mouse MX

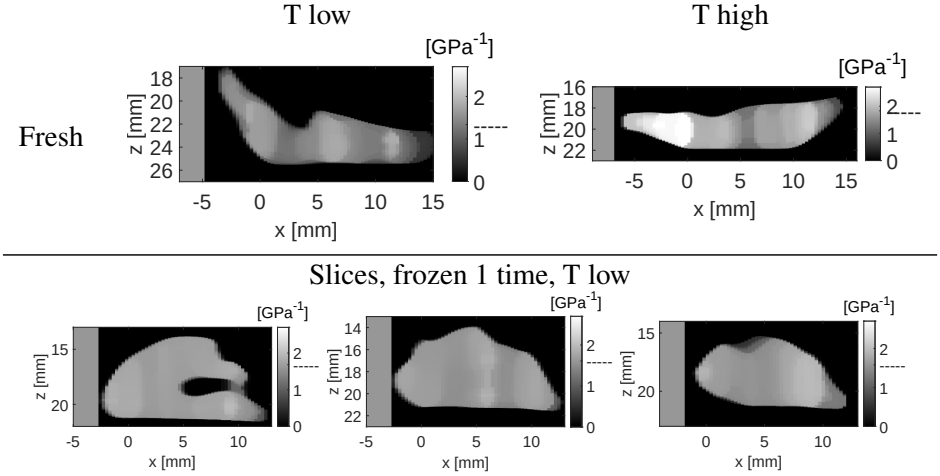

Table 6.14: Muscle, mouse MX

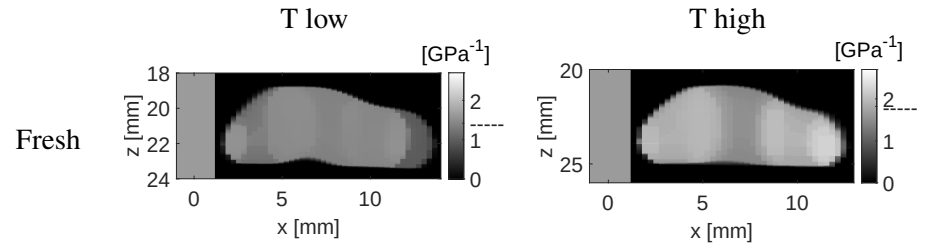

Table 6.15: Kidneys, mouse MY

	T low	T high
Fresh	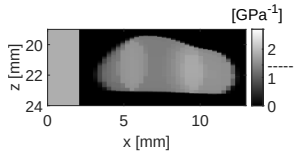	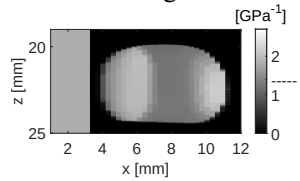
Fresh	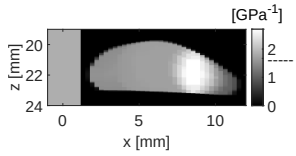	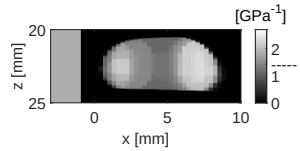
	T low	**T low (other slice)**
Frozen 1 time	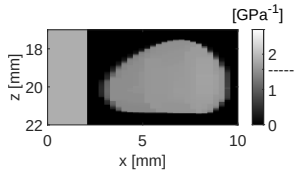	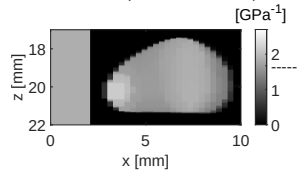

Table 6.16: Liver, mouse MY

	T low	T high
Fresh	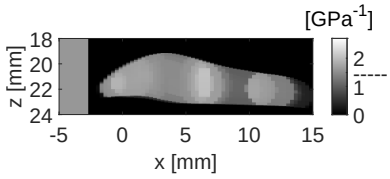	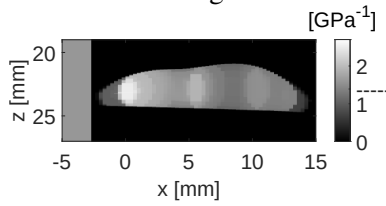
	T low	**T low (other slice)**
Frozen 1 time	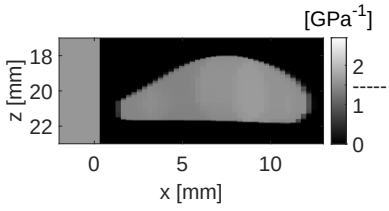	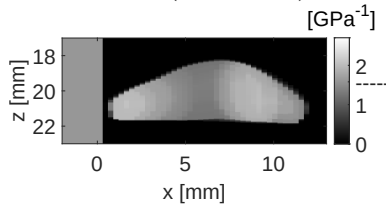

Table 6.17: Muscle, mouse MY

	T low	T high
Fresh	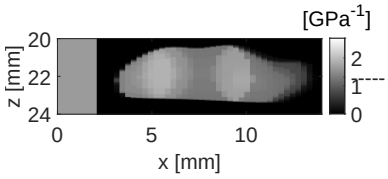	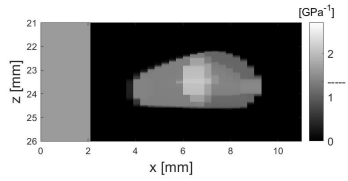

6.4.3 Effect of being frozen

The tumors and organs were kept in the freezer between each experiment. An interesting question was whether or not this has an impact on the β-value of the tumors. This was studied by measuring the same tumors under the same circumstances after being kept in the freezer a varying number of times. Fig. 6.11 shows β for tumors as a function of number of times being frozen. Fig. 6.12 shows β for organs as a function of number of times being frozen at low temperature (between 20 °C and 23 °C).

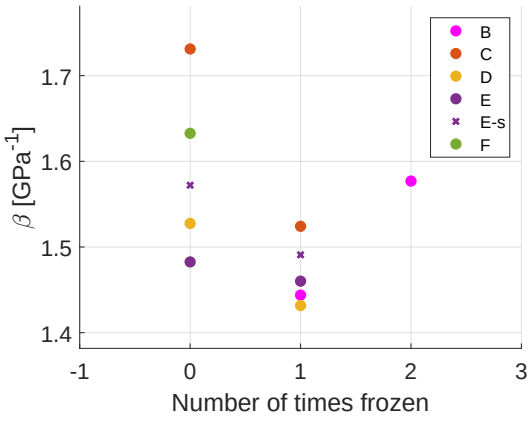

(a) T low

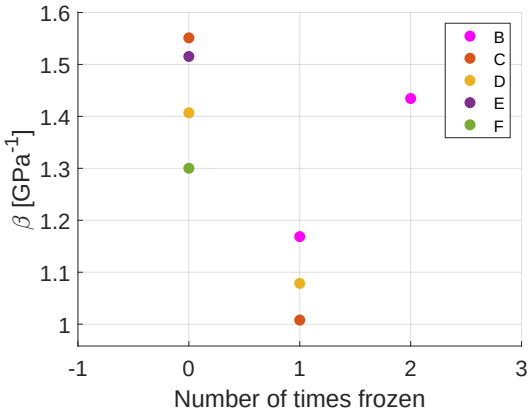

(b) T high

Figure 6.11: β as a function of number of times being frozen at low temperature. Each tumor has its own scatter type, labeled in the box in the plot. The "-s" refers to another slice of the tumor.

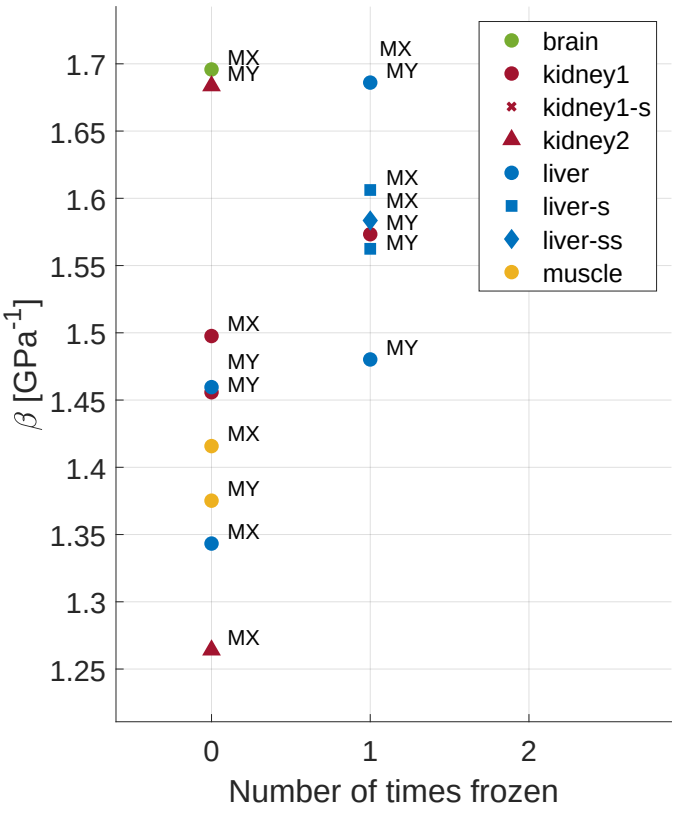

Figure 6.12: β as a function of number of times being frozen. Each organ has its own scatter type, labeled in the box in the plot. The "-s" and "-ss" refers to another slice of the same organ. The organs originate from the mice labeled next to the scatters.

6.4.4 Effect of varying temperature

To get an insight in how β depends on temperature, the tumors and organs were tempered to temperatures varying between 20-38 °C. Fig. 6.13 and Fig. 6.14 shows how β varies as a function of temperature, when the number of times being frozen is kept constant, for tumors and organs, respectively.

6.4.5 Slices

Different slices (layers) of both tumors and organs were measured to study the precision of the method. The layers are close to each other and the tissues are relatively homogeneous, such that the β value should be equal in the layers. The precision is calculated as 100 - mean of standard deviation [%] between the different slices of the same object. The mean standard deviation is interpreted as the uncertainty of the obtained β values. Both the mean standard deviation and the precision are given in Table 6.18. Fig. 6.15 shows two slices of tumor E (both fresh and frozen once), and Fig. 6.16 shows slices in different organs.

Table 6.18: Precision for tumors and organs.

	Mean standard deviation [%]	Precision [%]
Tumor	4.2	95.8
Organ	6.4	93.6

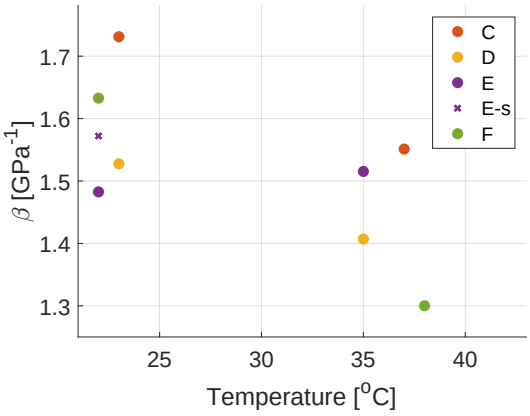

(a) Fresh

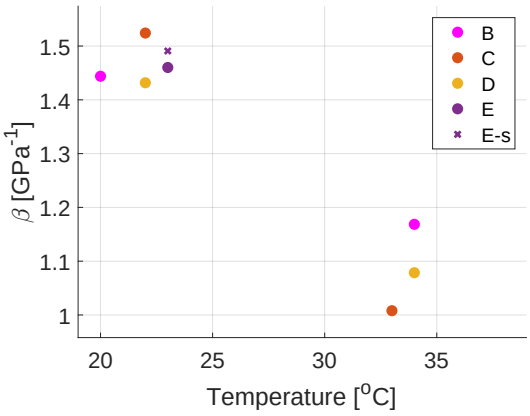

(b) Frozen once

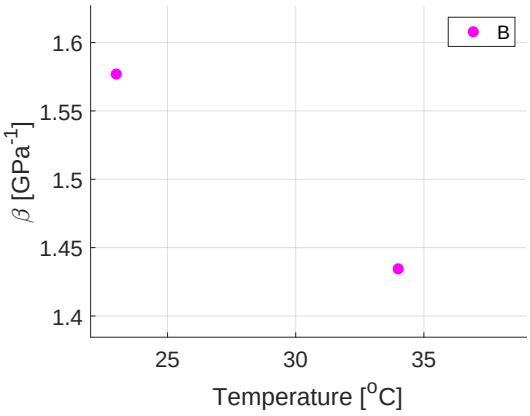

(c) Frozen twice

Figure 6.13: β as a function of temperature for tumors. Each tumor has its own scatter type, labeled in the box in the plot. The "-s" refers to another slice of the tumor.

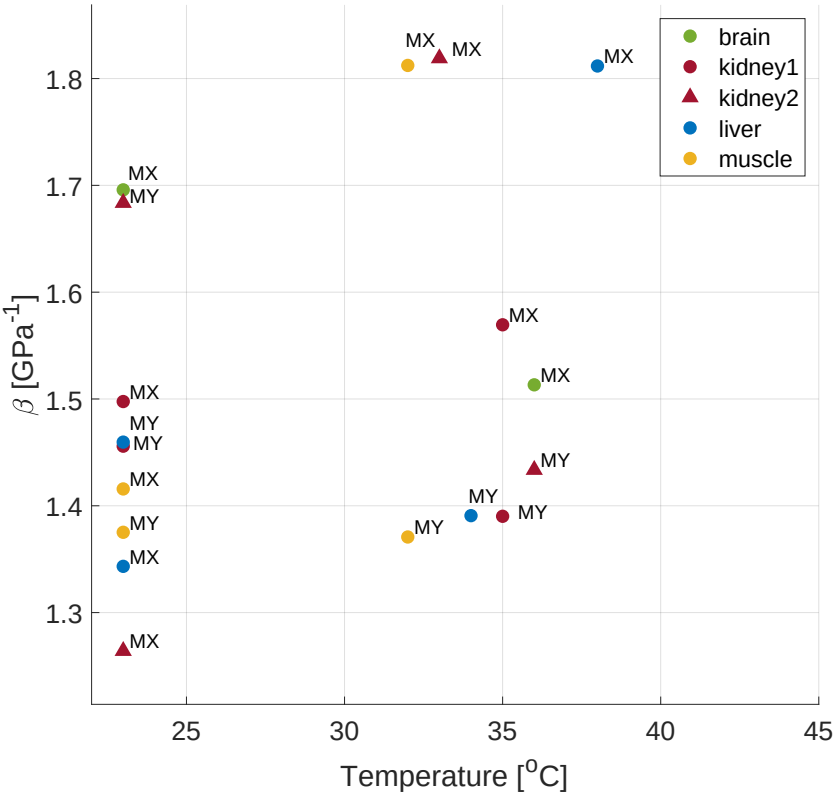

Figure 6.14: β as a function of temperature for fresh organs. Each organ has its own scatter type, labeled in the box in the plot. The organs originate from the mice labeled next to the scatters.

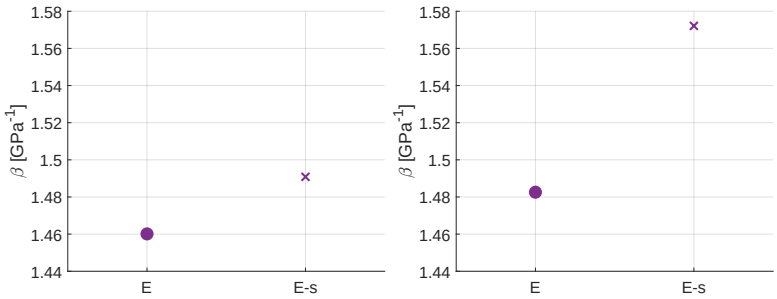

(a) Frozen 0 times **(b)** Frozen 1 time

Figure 6.15: Median β for two different slices of tumor E. The "-s" refers to another slice of the tumor.

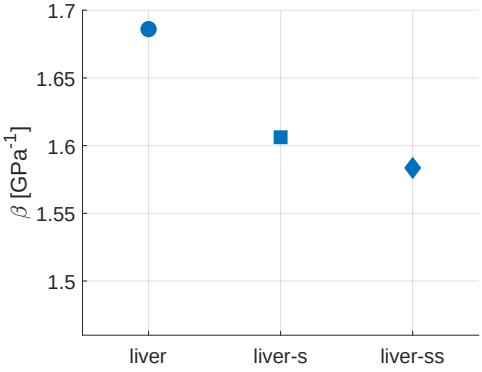

(a) Liver (frozen once), mouse MX.

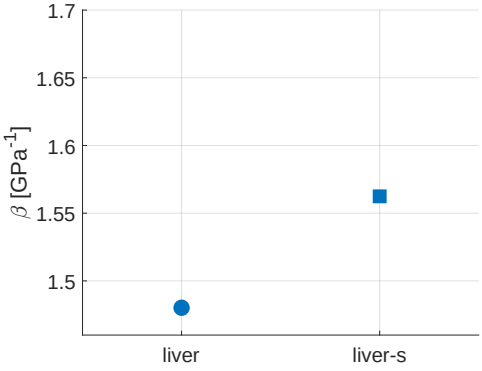

(b) Liver (frozen once), mouse MY.

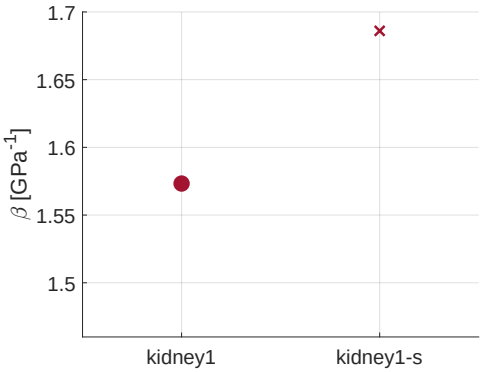

(c) Kidney (frozen once), mouse MY.

Figure 6.16: Median β for different slices of mouse organs. The "-s" and "-ss" refers another slice of the same organ.

Chapter 7

Discussion

In this chapter, the obtained results presented in Chapter 6 will be discussed.

7.1 Pre-results

All calculations made are based on RF signals from the Verasonics scanner. Section 6.1 shows results which are necessary to do the β estimation. Fig. 6.1 shows a conventional B-mode image, which is used to calculate weights to the model. From the B mode image one can find strong scatter, which are given higher weights. Fig. 6.2 shows the RF signal from one scan line for the two polarities (HF pulse located on a crest and HF located on a trough of the LF pulse). One can see that there is a delay between the two polarities. This is the basis for Fig. 6.3, which shows the delay for all scan lines. Fig. 6.4 shows the distance weight, which contains numbers between 0 and 1 based on how much we trust the data.

The very first tumor to be measured was tumor A and the results are shown in Table 6.2. This measurement was done in the middle of December and became a lesson of learning considering the experimental setup. First of all, the measurement made at 34 mm was too deep. Here, the delay τ is very inhomogeneous, resulting in an inhomogeneous β estimation. Furthermore, one can see a big change in β in the three images. This could be related to the temperature. The first measurement (depth 16 mm) was made a short time after the tumor was taken out of the freezer keeping -80 °C. The tumor was moved directly from the freezer to a box of distilled water. The temperature of the water was not measured. The second measurement was too deep (depth 34 mm), resulting in inhomogeneous results. When the third and last measurement was made, the tumor had been in the water for more than five minutes. According to the calculations made in Section 5.3, the tumor was

tempered at this point.

Tumor A became in many ways an effective lesson of learning for the later experiments. Even though the explicit results from this measurement have a low value, the experimental setup was optimized using the results. The take-home message was that the temperature might be important and should definitely be monitored, and the best depth is around 20 mm. In addition, the distilled water was changed to a NaCl 9 mg/ml solution for the later measurements.

7.2 Inhomogeneity

Before doing any measurements, the tumors were assumed to be homogeneous. However, the β estimate shows to vary inside some of the tumors when code version 2 is used. Examples are shown in Fig. 6.8. The question to be answered is whether this is related to the characteristics of the tumor, or the method for estimating β.

In tumor B (Fig. 6.8(a) one can see a darker spot above the brighter one. To study what cause such spatial variance Fig. 6.7 will be discussed. Here, the delay is shown in addition to the β estimate. The measured delay τ and the modeled delay τ_x through one scan line in the region of interest (shown as a red line in the images) reveal that the measured delay drops suddenly. This can also be observed as a dark area in the delay-image where the red line slices through. This drop in the delay is not expected as $|p_{LF}| > 0$ leading to an accumulative delay according to Eq. (4.4), such that this area should have a low distance weight. When the dark area above the bright area occurs in the β image, this is a strong indication of the distance weight being too big. When the distance weight is big, β is estimated as the gradient to the delay model according to Eq. (4.7). By observing the plot to the right in the figure, one can see that τ_x gets quite steep around depth 450, which results in a big gradient and a high β estimate. Before depth 450, on the other hand, τ_x might be too flat, which results in a too small estimate. This is why we see a dark area above the bright one in the β image. To summarize, the reason for this jump in the modeled delay τ_x is most likely to be an artefact rather than inhomogeneity inside the tumor. Possible artefacts will be discussed later in the chapter.

Tumor D (Fig. 6.8(b)) and tumor F (Fig. 6.8(b) have bright areas at the upper edge. These bright spots do also occur because of drops in the delay, similar to tumor B. In the experimental setup, it is only water on top of the tumor, such that none of the beams are scattered before arriving at the tumor. Hence, there is no reason for the delay being too small and it for sure is an artefact.

Based on these observations code version 3 was made. After the one iteration in the

solver, a modification of the weights is made. In areas where the measured NPD is much lower than the modeled NPD the weight is set to zero. A new iteration in the solver is made after the modification, and the non-expected inhomogeneities were removed as shown in Section 6.4.1.

7.3 Precision and accuracy

To validate the obtained results two methods were applied. First, β was measured on healthy mouse organs where literature values for comparison exist to get an impression of the accuracy. Secondly, slices with no more than 2 mm difference in the distance were measured on the same object to get an impression of the precision as we assume homogeneity in the object.

7.3.1 Accuracy

Section 6.4.2 shows the results from measurements made on healthy mouse tissues. The literature values used for comparison are shown on the left side in the figures and originate from Mast (2000). The values correspond to human tissues and the temperature is not specified. It is assumed that the data was collected *in vitro*. The literature values are therefore compared to both results from different temperatures as well as for fresh organs and organs which have been frozen. The box plot presented in Fig. 6.10 summarize the findings in a easy-reference way, and the calculated accuracies are given in Table 6.10.

The results accord most with the literature values at low temperatures after the organs have been frozen once, with an accuracy of 93.9 %. As a consequence of this, the β values obtained for the tumors in this setting (T low, f1) may be handled as the most correct value.

The organs were removed from the mice, such that some additional tissues surrounding the organ were present. Fat was present on the piece of muscle and also on the kidneys, and might be the reason for the variance in the β values (as fat stands out with a high β value compared to the other tissues). One can see the big variation in the box plot in Fig. 6.10. The data from kidneys are also based on twice as much data as the other tissues, as both mice have two kidneys. This may also be an explanation of the larger span between the first and third quantile in the box plot.

It should be mentioned that "kidney1" and "kidney2" might have been swapped during the measurements at different temperatures and after being frozen. For this reason, "kidney1" and "kindey2" should be interpreted as common values in Fig. 6.12 and Fig. 6.14. This is reasonable to do as the kidneys are similar and should have equal β values anyhow.

7.3.2 Precision

Tumor E, liver from both mice, and kidneys from mouse MY were used to calculate the precision of the method. Both the tumor and the chosen organs are assumed to be relatively homogeneous.

To slices of tumor E are shown in Table 6.7, and the median values are plotted in Fig. 6.15. One can see that the values differ more when the tumor has been frozen once, but the difference is still less than 0.1 GPa^{-1}. Such a small difference is hard to spot in the β images which make the result acceptable.

The median values for the organ slices are plotted in Fig. 6.16. Again, the maximum difference is around 0.1 GPa^{-1}. The kidneys vary the most, which might be caused by the structure of the kidney itself. The kidneys are treated as homogeneous, but in reality the kidneys consist of layers with different stiffness which of course have an impact on the β value in different slices.

In total, the precision was calculated to be 95.9 % for tumors and 93.6 % for organs (given in Table 6.18).

7.4 Temperature

To get an insight in how β is affected by temperature, measurements on the tumors were made at varying temperatures between 20 °C and 38 °C, which is the span from room temperature to body temperature. Fig. 6.13 and Fig. 6.14 shows median value of estimated β values for all measurements on tumors and organs, respectively.

For tumors, the trend when the temperature increase is a decrease in β. This can be observed by studying the same tumor at the two temperatures, i.e the same scatter type in each of the plots. The drop varies from approximately 0.1 GPa^{-1} for tumor D (fresh) to approximately 0.5 GPa^{-1} for tumor C (frozen once). The only exception is tumor E (fresh) where β increases when temperature increase, but the difference is within the precision of the method.

The measurements made at high temperatures on tumors which have been frozen one time resulted in a noticeable low β estimate. This may indicate that the temperature dependency is more significant after being frozen. The variety of the estimates are similar to the other measurements, which strengthens the argument.

A decrease of β when temperature increase is reasonable because the material density decrease.

For organs, different results are observed. Muscle, liver and kidney2 from mouse

MX stand out with an increase higher than 0.3 GPa^{-1} when the temperature increase from low to high. The occurrence of fat on the tissues was discussed as one source of error in the previous section. The box plot obtained for tumors does also indicate that the β value is more affected by a change in temperature after the object has been frozen. Data from organs at high temperatures after being frozen is not collected, such that the statement is based on data from tumors. However, this may explain the lack of trend for the organs in mouse MX.

For mouse MY, the same decrease in β is observed when the temperature increase as for tumors. The decrease is however within the range of precision, such that it is hard to draw any conclusion.

7.5 Effect of being frozen

It was studied whether or not the β value is affected if the tumor or organ has been frozen. The median values of β as a function of number of times being frozen are shown in Fig. 6.11 and Fig. 6.12 for tumors and organs, respectively.

The β value tend to decrease when the tumor has been frozen once, both for the low and high temperatures. The difference varies from 0.05 GPa^{-1} for tumor D at high temperature to 0.55 GPa^{-1} for tumor C at low temperature. Once again, tumor C varies the most in the same way as for the β vs temperature plot (Fig. 6.13).

Tumor C stood out as the most varying tumor considering changes in temperature and the number of times being frozen. The β estimates shown in Fig. 6.5 shows a very smooth and homogeneous estimate throughout the whole tumor, which makes the deviation even harder to explain.

Tumor B was also measured after being frozen twice, and the median β value does increase. This is the same trend as for organs, shown in Fig. 6.12. However, the values here are more cohesive which opens the possibility of no trend at all, meaning that β is independent of the number of times the object has been frozen. This is also more reasonable as the density is the same when the object has been frozen or not (when tempered again, of course).

It can not be excluded that the amount of time being in the freezer is irrelevant either. For these measurements, the time spent in the freezer was always less than a month in total. It is likely that the structure and hence the β value changes even more if the tumor is placed in the freezer for a longer time.

7.6 Uncertainty

With all technology and methods comes uncertainty and potential for improvement, and the SURF method is no exception.

7.6.1 Broken transducer element

The first thing to be mentioned is the artefact occurring as a result of one broken element in the transducer. This can easily be observed in the modeled LF field shown in Fig 4.4 where the pressure is low in the region x $\in$ (-10,-5) mm. To avoid errors as a consequence of this broken element, the object to be imaged can be placed in a region with functioning elements only. This is the reason why the tumors and organs are located to the right in all images.

7.6.2 Unexpected drops of measured delay

In the delay-images darker areas inside the tumor sometimes occur. These are unexpected drops of the measured delay. One example is in Fig. 6.3 at z $\approx$ 20 mm and x $\approx$ 8 mm in Fig. 6.3. These are artefacts occurring for some unknown reason. Some possibilities are side-lobes, speckle or reverberation, and will be discussed later.

Such darker areas have a huge impact on the delay model which in turn affects the β estimate. To account for such dark areas, the distance weight in the estimation functional should have a zero weight. This was also the modification made from version 2 to version 3 in the code. By setting the distance weight to zero in these areas, β is estimated based on regression between neighboring estimates rather than a local estimate. Without this weight, the estimate would have been too low initially and too high at the end as the gradient is near zero inside the dark area and makes a "jump" at the end of the dark area. Tumor B is a good example of this artefact, and the β estimate and weights for the two versions are shown Table 7.1 for comparison. The bright spot is removed in version 3 because the weight is changed to zero there.

7.6.3 How good is the method

The average β value found for tumors are given in Table 6.3 and differ from tissue values shown in Fig. 6.10, such that in theory it should be possible to detect tumors in tissue.

The accuracy and precision of the method are at the best 93.9 % and 95.8 %, respectively. Another part of the method which affects the accuracy is the LF pressure model. As mentioned in section 7.2, inhomogeneities in the LF field may be the reason for the sudden delay drops occurring in some of the measurements.

Table 7.1: Comparison between version 2 and version 3 for tumor B being frozen once at 20 °C

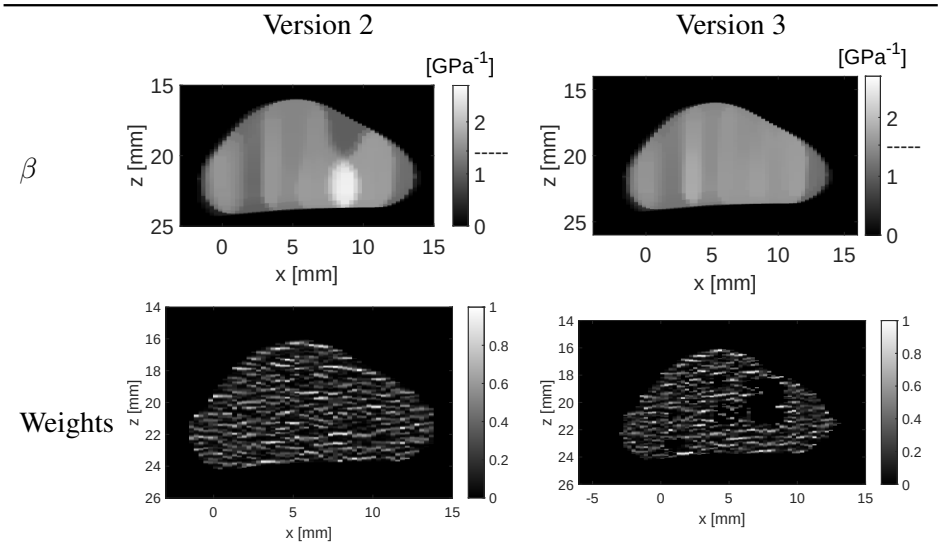

Again, the LF pressure is modeled based on measurements from a water tank and does not give a homogeneous manipulation of the HF pulse, as desired. As the surroundings were very controlled in this experiment, with only water and a strong reflector at the bottom in addition to the object to be imaged, it is reasonable to believe that most of the variation in the results occur as a consequence of the LF pressure. This can, however, not be concluded until another LF pressure is examined.

In this experimental setup, the level of noise is low because water does not scatter. More noise will occur for *in vivo* measurements.

7.6.4 Artefacts

Reverberation

Reverberation is an artifact occurring when the ultrasound beams encounter two parallel strong reflectors, such that the beams are reverberated back and forth between the reflectors Blüthgen et al. (2017). This leads to a longer arrival time for the beam such that the reflector is interpreted as being deeper than its true location.

For the specific setup with an object in a box of water, reverberation is not a big problem. In a more realistic case where patients are being imaged, cross-beam can be used to minimize or eliminate reverberation signals. Theoretically, the bigger

angle (up to 90°) the better, but this is a limitation if only one array is used. As mentioned, reverberation in the experimental setup used here and receive cross beams are therefore not necessary.

Side-lobes

Side-lobe artefacts occur if the side lobes of the main ultrasound beam are reflected and the echo is displayed as if it originates from the main beam. The bottom in this experimental setup is one example of a strong reflector and may therefore disturb the β estimation. To account for this, the bottom is removed aggressively, meaning that the tumor is segmented and even one millimeter above what is interpreted as the bottom is removed. Before adding this safety millimeter, part of the bottom was included in the estimate for some tumors. A remarkable decrease of β was observed and highlighted the effect of removing the bottom completely. The tumor itself is also a strong reflector compared to the surrounding water solution in this experimental setup. One can see some side-lobe artefacts in Fig. 6.3 on the sides of the tumor. The areas outside the tumor will be filtered away, but if the artefacts appear inside the tumor the focus is to have a low distance weight in these areas. The dark areas inside the tumor may be side lobe artefacts.

Speckle

Speckle artefacts are caused as the reflected beams interfere with each other. The easiest way to observe speckle noise is in the B mode image, as speckle gives a grainy look. However, the artefact is present in all the processed data, as all calculations are based on the echo signals which are interfered. The speckle artefact can be observed in the solution surrounding the tumor in Fig. 6.3.

Chapter 8

Conclusion

The nonlinear bulk elasticity β for PDAC tumors and healthy organs from KPC mice and has been estimated using *in vitro* dual frequency ultrasound.

The average value of all tumors was estimated to be 1.53 GPa^{-1} at room temperature and 1.31 GPa^{-1} at temperatures between 30 °C and 38 °C (a rough approximation of body temperatures). By comparing estimates from nearby layers in a tumor, the precision was calculated to be 95.8 %. The results showed that β decreased as the temperature increase for the tumors.

For the healthy tissues at room temperature, average β value was estimated to be 1.53 GPa^{-1}, 1.70 GPa^{-1}, 1.53 GPa^{-1} and 1.40 GPa^{-1} for liver, brain, kidney, and skeletal muscle, respectively. At temperatures between 30°C and 38 °C, the average β value was estimated to be 1.60 GPa^{-1}, 1.51 GPa^{-1}, 1.55 GPa^{-1} and 1.59 GPa^{-1} for liver, brain, kidney, and skeletal muscle, respectively. The accuracy of the method varied between 87.0% and 93.9%, and was found by comparing the estimated β values for healthy organs with literature values from human organs.

The nonlinear bulk elasticity for tumors is somewhat lower than the nonlinear bulk elasticity for healthy tissues at temperatures between 30 °C and 38 °C, which suggests that tumors may show contrast to healthy tissues for *in vivo* measurements.

8.1 Future work

In this thesis, it has been shown that the nonlinear bulk elasticity for tumors is somewhat lower than the nonlinear bulk elasticity for healthy tissues at temperatures between 30 °C and 38 °C. This indicates that the imaging technique has big potential.

A suggestion for improvement of the estimation of NEP is to optimize multiple scan lines together, instead of optimizing each line individually. In addition, the weights are made for the "object in a box of water"-case, such can therefore be made more general.

It remains to do in vivo measurements. I got the opportunity to join and take part in *in vivo* experiments on mice. This was beyond the scope of my thesis and is therefore not included. However, it was exciting to get a taste of the next step in the work.

Even further into the future, *in vivo* measurements on humans will be made. It will be exciting to see whether or not the technique can be used for tumor detection and characterization.

Bibliography

Fahrudin Smajlovic Aladin Carovac and Dzelaludin Junuzovic. Application of ultrasound in medicine. *Academy of medical sciences of Bosnia and Herzegovina*, ():168–171, 2011. doi: {10.5455/aim.2011.19.168-171}.

Bjørn A J Angelsen and Rune Hansen. 7a-1 surf imaging - a new method for ultrasound contrast agent imaging. pages 531–541, 2007. doi: 10.1109/ULTSYM.2007.140.

Robert Beyer. Parameter of nonlinearity in fluids. *The Journal of the Acoustical Society of America*, 32(719):, 1960. doi: {10.1121/1.1908195}.

Christian Blüthgen, Sergio Sanabria, Thomas Frauenfelder, Volker Klingmüller, and Marga Rominger. Economical sponge phantom for teaching, understanding, and researching a- and b-line reverberation artifacts in lung ultrasound. *Journal of Ultrasound in Medicine*, 36, 2017. doi: {10.1002/jum.14266}.

Ole Martin Brende. *Reverberation suppression with dual band imaging in medical ultrasound*. PhD thesis, Norwegian University of Science and Technology, Trondheim, June 2015.

Cancer Registry of Norway. Cancer in norway 2019 - cancer incidence, mortality, survival and prevalence in norway. *Oslo: Cancer Registry of Norway*, 2020.

F. Fox and W. Wallace. Absorption of finite amplitude sound waves. *The Journal of the Acoustical Society of America*, 26(994):, 1954. doi: {10.1121/1.1907468}.

Rune Hansen, Svein-Erik Måsøy, Tonni F. Johansen, and Bjørn A J Angelsen. Utilizing dual frequency band transmit pulse complexes in medical ultrasound imaging. *The Journal of the Acoustical Society of America*, 127(1), 2010. doi: {10.1121/1.3257584}.

Rune Hansen, Svein-Erik Måsøy, Thor A. Tangen, and Bjørn A J Angelsen. Nonlinear propagation delay and pulse distortion resulting from dual frequency band transmit pulse complexes. *The Journal of the Acoustical Society of America 1*, 129(2), 2011. doi: {10.1121/1.3518753}.

Jeff Hardin and Gregory bertoni. *Becker's World of the Cell, 9th edition*. Pearson, May 30, 2017.

O. Hassan, Noha Hassan, and Yasser Kadah. Modeling of ultrasound hyperthermia treatment of breast tumors. *National Radio Science Conference, NRSC, Proceedings*, 01 2009.

Jørgen Arendt Jensen. *Estimation of Blood Velocities Using Ultrasound: A Signal Processing Approach, 3rd release*. Cambridge University Press, August 30, 2013.

Johannes Kvam, Stian Solberg, Ola F. Myhre, Alfonso Rodriguez-Molares, and Bjørn A J Angelsen. Nonlinear bulk elasticity imaging using dual frequency ultrasound. *The Journal of the Acoustical Society of America*, 146(4), 2019. doi: {10.1121/1.5129120}.

T Douglas Mast. Empirical relationships between acoustic parameters in human soft tissues. *Acoustics Research Letters Online-arlo - ACOUST RES LETT ONLINE-ARLO*, 1, 11 2000. doi: 10.1121/1.1336896.

National Cancer Institute. Types of cancer treatment. `https://www.cancer.gov/about-cancer/treatment/types`. Accessed: 2021-05-08.

National Cancer Institute. Cancer statistics. `https://www.cancer.gov/about-cancer/understanding/statistics`, 2020. Accessed: 2021-01-21.

Krister Svanberg. A class of globally convergent optimization methods based on conservative convex separable approximations. *SIAM Journal on Optimization*, pages 555–573.

Laura Vroling, Yuana Yuana, Gerrit Jan Schuurhuis, Victor van Hinsbergh, Chad Gundy, Richard Haas, Hester Cruijsen, Epie Boven, Klaas Hoekman, and Henk Broxterman. Vegfr2 expressing circulating (progenitor) cell populations in volunteers and cancer patients. *Thrombosis and haemostasis*, 08 2007.

World Health Organization. Screening and early detection. `https://www.euro.who.int/en/health-topics/noncommunicable-diseases/cancer/policy/screening-and-early-detection`. Accessed: 2021-05-08.

Lang Xia. Analysis of acoustic nonlinearity parameter b/a in liquids containing ultrasound contrast agents. *The Journal of the Acoustical Society of America*, 146(1394):, 2019. doi: {10.1121/1.5123486}.

Ping Yuan. Numerical analysis of an equivalent heat transfer coefficient in a porous model for simulating a biological tissue in a hyperthermia therapy. *International Journal of Heat and Mass Transfer*, 52(7):1734–1740, 2009. doi: {0.1016/j.ijheatmasstransfer.2008.09.033}.

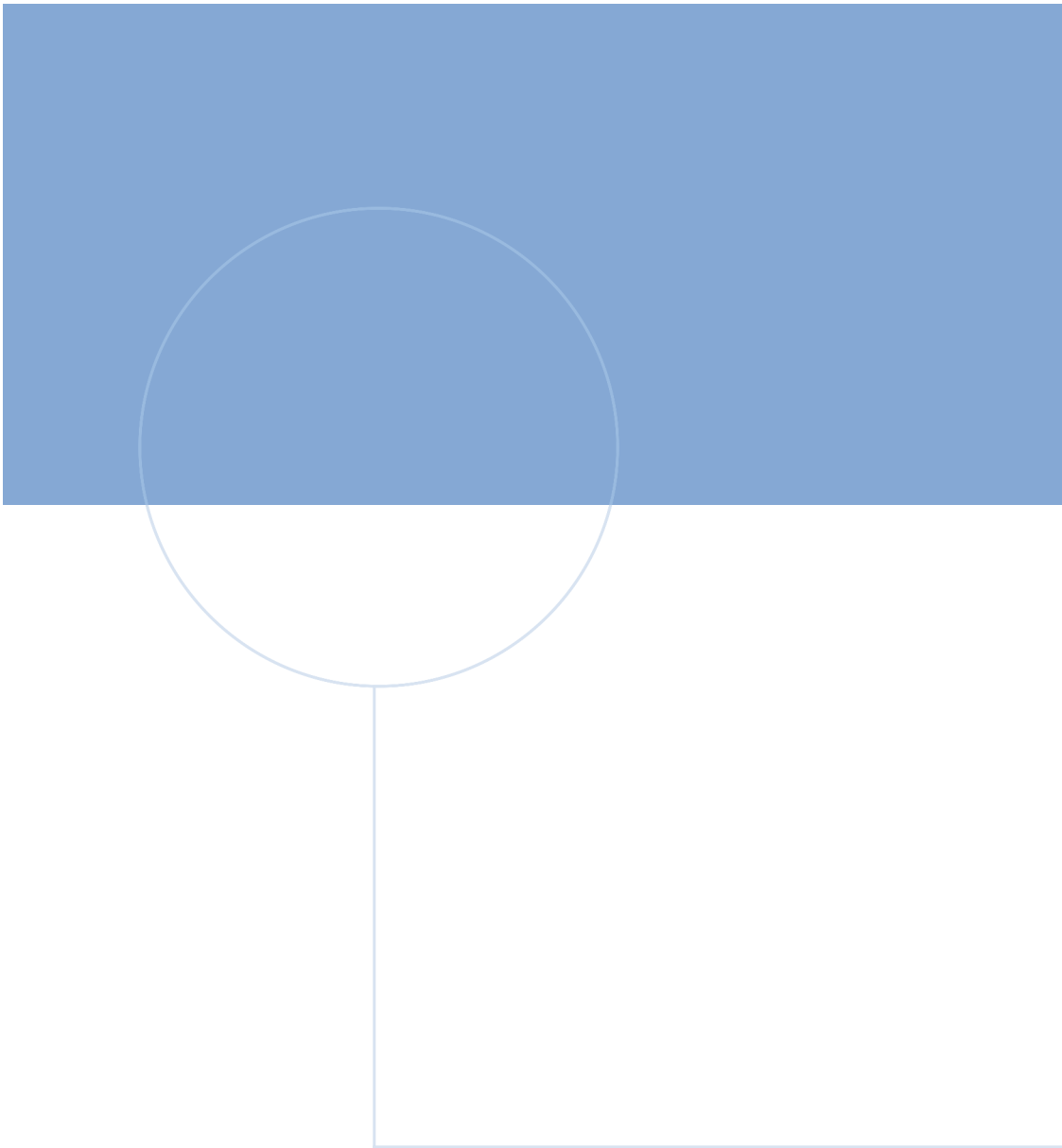

NTNU

Norwegian University of
Science and Technology